Distribution
Category UC-70

SAND87-7070

Unlimited Release
Printed August 1988

HYDROLOGIC MODELING OF VERTICAL AND LATERAL MOVEMENT OF PARTIALLY SATURATED FLUID FLOW NEAR A FAULT ZONE AT YUCCA MOUNTAIN

by

J. S. Y. Wang and T. N. Narasimhan

Earth Sciences Division
Lawrence Berkeley Laboratory
University of California
Berkeley, CA 94720

for

Sandia National Laboratories
Albuquerque, NM 87185
Sandia Contract: 64-5958

ABSTRACT

Distribution of fluid flow is governed by the balance between gravity and capillary forces. The objective of this work is to assess fluid flow in the partially saturated, fractured, porous tuff formations at Yucca Mountain. The effects of eastern tilting of the units at Yucca Mountain on fluid flow has been studied using two-dimensional models. Ghost Dance Fault has been modeled as a seepage face. Under the expected flux conditions, saturation increased just to the west of the fault, but the water did not enter the fault. Tuff matrix and fracture data have been compared to the limited model parameters of the fault; and correlations between saturated conductivity and unsaturated parameters for tuff matrix, fracture, and fault are discussed.

CONTENTS

FIGURES
(continued)

TABLES

ACKNOWLEDGMENTS

We thank S. Sinnock, P. G. Kaplan, and Y. T. Lin for discussing the simulations; R. R. Peters, R. Eaton, P. Hopkins, D. McTigue, K. Pruess, Y. Tsang, and G. Bodvarsson for reviewing the manuscript; and M. Alavi for assisting with the plottings. This work was supported by Sandia National Laboratories for the Nevada Nuclear Waste Storage Investigations Project of the U.S. Department of Energy.

NOMENCLATURE

a_v	compressibility	$[M^{-1}Lt^2]$
$\bar{b}$	effective aperture	[L]
b_c	contact cutoff aperture	[L]
D	fracture spacing	[L]
h	pressure head	[L]
k(S)	permeability at saturation S	$[L^2]$
K_s	saturated permeability	$[L^2]$
m	parameter in van Genuchten's formula, $m = 1 - 1/n$	
n	parameter in van Genuchten's formula	
S	saturation	
t	time	[t]
α	parameter in van Genuchten's formula	$[L^{-1}]$
ϕ	porosity	
ω	fraction of surface contact area	

van Genuchten's formula:

$$S = S_r + (1-S_r)\left[\frac{1}{1 + (-\alpha h)^n}\right]^m$$

$$\frac{k(S)}{k_s} = \frac{(1 - (-\alpha h)^{n-1}\,[1 + (-\alpha h)^n]^{-m})^2}{[1 + (-\alpha h)^n]^{\frac{m}{2}}}$$

1.0 INTRODUCTION

The work described in this report was performed for Sandia National Laboratories as a part of the Nevada Nuclear Waste Storage Investigations Project. The NNWSI Project is administered by the Nevada Operations Office of the Department of Energy. The project is part of the DOE's program to dispose safely of the commercial high-level nuclear wastes. The NNWSI Project is evaluating the suitability of Yucca Mountain, on and adjacent to the Nevada Test Site in southern Nevada, to determine the feasibility of developing a mined repository for high-level nuclear wastes.

The objective of this work is to aid performance assessment activities at SNL by modeling the fluid flow in partially saturated, fractured, porous tuff formations at Yucca Mountain. The distribution of fluid flow is governed by the balance between gravity and capillary forces. The external gravitational force moves the water downward, and the internal capillary forces hold the water in place within the pores. The magnitude of the capillary force is inversely proportional to pore size, and the heterogeneity of rock pore structure controls distribution and movement of water through partially saturated formations. Within the centimeter scale of an unfractured tuff rock sample amenable to conventional laboratory measurements, the pore size distribution determines the characteristic curve of the degree of saturation as a function of suction pressure. The characteristic curve describes the percentage of saturated small pores and unsaturated large pores in response to a given external suction force. On the meter scale of tuff matrix blocks separated by discrete fractures, the fractures represent openings with average apertures much larger than the average pore sizes of the matrix. Except near the contact areas between two rough fracture surfaces, most fracture openings cannot maintain the strong capillary forces required to hold water within the fractures under ambient partially saturated conditions.

In the first phase of this study, we developed a conceptual model and constructed a general statistical approach for analyzing the flow of water along fractures and between matrix blocks and adjoining fractures under partially saturated conditions (Wang and Narasimhan, 1985). Characteristic curves for fractures were derived from data on fracture spacings, orientations, contact fractions, and bulk formation conductivity. Analyses of gravity drainage through a vertical heterogeneous column of tuff using the previously mentioned characteristic curves and explicitly treating the fractures and matrix blocks indicate that steady-state fluid flow within Topopah Spring Member, the candidate host rock for the repository, occurs mainly through the partially saturated rock matrix. These results are entirely consistent with the general capillary mechanism, with large pores, including fractures easily drained, and with small pores holding the water. An understanding of the drastic change in the role of fractures from active main conduits for the flow and transport of water under saturated conditions to passive dry pores under unsaturated conditions is crucial for assessment of the partially saturated fluid flow field at Yucca Mountain, which is hundreds of meters thick and several square kilometers in area.

Yucca Mountain consists of alternating units of welded and nonwelded tuff (Ortiz et al., 1984). The candidate Topopah Spring Member is a

fractured, welded unit approximately 300-m thick bounded above and below by nonwelded units several tens of meters thick. In the second phase, we studied the effect of the upper nonwelded Paintbrush unit (PTn) on infiltration. This study simulated the injection of water into a vertical column in the PTN unit sandwiched between a 10-m section of the welded Tiva Canyon unit (TCw) above and a 10-m section of the welded Topopah Spring unit (TSw) below. We also studied the effect of both nonwelded units on a long column from the ground surface (GRD) to the water table (WT), covering the entire partially saturated zone from the top down through the TCw unit, the PTn unit, the TSw unit, the Calico Hills nonwelded, vitric unit (CHnv), and the Calico Hills nonwelded, zeolitic unit (CHnz). Different constant and pulse infiltration rates were applied to fractures at the top of the columns to determine spatial and temporal distributions of water movement through partially saturated units. Large variations of saturation, pressure, and potential distributions occurred mainly near the interfaces between the welded and nonwelded units. Different characteristic curves resulting from different pore and fracture size distributions among the units will adjust differently to imposed infiltration and gravitational force across the interfaces. Most pulse effects are effectively damped out by the top two units before water infiltrates down into the Topopah Spring Member (Wang and Narasimhan, 1986).

In the third phase of this study, the model was extended laterally to a 1,000-m two-dimensional cross section bounded by vertical fault zones. Earlier single-vertical-column models assumed that the average fluid flow direction is vertical. If the interfaces of the alternating units are horizontal, the vertical flow pattern is expected based on symmetry considerations. The stratigraphic units at Yucca Mountain generally tilt 5° to 7° eastward (Scott and Bonk, 1984). Several investigations have suggested that a lateral component of the gravity gradient, caused by the tilt may divert some water laterally to a high-conductivity fault zone where a vertical flow of the diverted water can continue (Montazer and Wilson, 1984; Rulon et al., 1986). If a substantial fraction of the net infiltration could be diverted away from dispersed vertical flows through unsaturated units to a concentrated flow through a localized fault zone, the fault zone would likely constitute the fastest flow path from the repository to the WT. In saturated systems an open fault with high conductivity is indeed likely to be the main conduit for fluid flow. However, the high saturated conductivity also implies that equivalent pores of the fault zone are larger than characteristic pores of the formations. If we assume that the same capillary mechanism governing meter-scale fracture-matrix blocks is applicable to the much larger fault-formation units, we may argue that the fault zone will be dry and water will remain in the tuff units. The capillary mechanism can be applied only to systems with pores small enough to maintain a meniscus between rock surfaces. Without experimental studies of the unsaturated characteristics of fault zone material, we cannot exclude other flow patterns, such as sheet flow, to effectively transport fluid along a fault surface to the WT. In this study, we will not address the question of how fast water can travel along a fault. We will instead focus our attention on whether water can overcome capillary forces holding it in the unsaturated units and exit laterally through formation-fault interfaces. Once water leaves the formation, we assume that it will fall freely down to the WT. Instead of modeling the

fault zone explicitly, we treat the formation-fault interface as a seepage boundary.

It is assumed that the fault is so open that the face of the fault behaves like an open surface exposed to atmospheric pressure. It is well known in hillside studies that water will seep out of formations if the potential at the open face boundary is lower than the potential inside the hill. If the potential near formation-fault interfaces can be increased to initiate seepage flow, then the fault zone could become an important flow channel. On the other hand, if seepage flow cannot be initiated or seepage flow magnitude is very small, then the predominant flow pattern will remain vertically downward within the unsaturated units.

2.0 HYDROLOGIC MODELS

We will model the behavior of partially saturated fluid flow through portions of formation units in Section A-A'. Section A-A' cuts through the central portion of Yucca Mountain as shown in Figure 1 (SNL, Product CAL0119). The vertical cross section of A-A' as given by the Interactive Graphics Information Services is shown in Figure 2 (SNL, Product CAL0115). A minor fault inside the proposed repository area, Ghost Dance Fault (GDF), will be a major hydrologic concern if fault flow is an important transport mechanism. To focus on the impact of GDF on the two-dimensional flow behavior, we have modeled the region west of GDF, treating GDF as an eastern seepage boundary. The location of the western no-flow boundary is treated as a variable, a few hundred meters to over half of 1,266.5 m, which corresponds to the Solitario Canyon (SC) boundary. The unsaturated region is bounded on the top by the GRD and on the bottom by the WT. To focus on the effect of tilting of the interfaces on fluid flow, Section A-A' has been simplified by neglecting the topographic variations of the GRD and treating the GDF boundary as vertical. We have also assumed that all interfaces tilt by 6°. The unit thicknesses used in the two-dimensional meshes are summarized in Table 1. Most thicknesses correspond to the Reference Information Base (RIB) digitized grid at GDF. The thickness of the TCw unit corresponds to the thickness below a topographic low west of GDF. The thicknesses of the Crater Flat Upper nonwelded unit (CFUn) and Bullfrog welded unit (BFw) were chosen to yield the same interface positions as the digitized grid crossing the WT near the western SC boundary. Table 1 also includes the tilting angles of the different units calculated from differences in digitized GDF and SC elevations.

The baseline matrix properties used in the models are summarized in Table 2. Saturated matrix conductivity, porosity, and residual saturation values were taken from Montazer and Wilson (1984) when the data were tabulated and from Sinnock et al. (1984) and Peters et al. (1984) for the TCw and PTn units. The saturated conductivity values taken from the RIB for the TSw and Calico Hills units are lower than the corresponding values in earlier references. All characteristic curves (van Genuchten parameters) are deduced from Peters et al. (1984). TSw1, TSw2, CHnz, and the Prow Pass welded unit (PPw) values correspond to representative samples chosen by Peters et al. (1984). PTn values correspond to sample USW G4-2, and CHnv values correspond to sample USW GU3-15. Characteristic curves for these

two samples correspond to wider pore size distributions than other samples of the two nonwelded units. Recent laboratory wetting experiments and scanning electron microscopic studies of PTn samples indicate that nonwelded tuff has a multimodal pore structure that can be measured by mercury intrusion and a psychrometer for different pore sizes (Peters et al., 1986a). The PTn USW G4-2 sample is one of the few samples for which mercury intrusion data and psychrometer data are relatively close to each other (Peters et al., Appendix C, 1984). Geologic logs also indicate that the nonwelded units are in general more heterogeneous than the welded units. Therefore, characteristic curves representing wider pore size distributions may be more appropriate in modeling these units. For the lower units (CFUn and BFw), average values are used for the van Genuchten parameters of the few samples from these units (Peters et al., 1984).

The fracture properties are also updated in Table 3. Average fracture orientation and frequency data from five boreholes (Bauer, 1987) together with bulk saturated formation conductivity from Well J-13 (Winograd and Thordarsson, 1974; Thordarsson, 1983; Sinnock et al., 1984) are used to deduce the fracture characteristic curves (Wang and Narasimhan, 1985). The main difference between the updated results of the average fracture geometry data and the early analyses of the USW G-4 data is that there are relatively fewer horizontal fractures than vertical fractures, especially in the welded units. Fractions of fracture surfaces where adjoining matrix blocks are in contact are assumed to be identical to fractions of areas where mineral coatings occur in fracture cores. The USW G-4 data (Spengler and Chornack, 1984) are used to estimate these contact fractions and determine the fracture contact cutoff apertures (Wang and Narasimhan, 1985).

3.0 VERTICAL INFILTRATION

First, we will review and discuss the results of a one-dimensional vertical infiltration through a column. The stratigraphy of the column corresponds to the units above the WT at GDF (Table 1). To properly model saturation, pressure, potential, and velocity variations, each unit is divided into grids. The grid spacings are summarized in Table 4. The results using a coarse grid are compared to the results using a fine grid in Figure 3. For the coarse grid, each unit is divided uniformly into several equal-thickness subunits. A general guideline for choosing the number of divisions is that the pressure or potential values between neighboring grid points are within 10 m of the hydraulic head. An explicit integration procedure (Narasimhan et al., 1985; Wang and Narasimhan, 1986) is used to estimate the one-dimensional pressure distributions for given infiltration rates and to aid mesh designs. For the fine grid, each unit has a nonuniform mesh with fine grids near the interfaces between different units. As the distance from the interface increases, the grid gradually increases in size with the ratio of the grid size no larger than a given magnitude w, where $w = (10)^{0.25}$. For the fine, nonuniform grid, we also checked conductivity and flux values in an explicit integration procedure to fine tune the mesh design before the mesh and initial estimate of potential distribution were used in the implicit numerical code TRUST (Narasimhan et al., 1978). The fine grid was used for both 0.1- and 0.5-mm/yr infiltration rates and for columns at other locations in Section A-A'.

Different mesh designs were tested systematically under different conditions before the two-dimensional meshes were constructed so that the basic one-dimensional columns would not introduce inaccuracies in the computations. Because columns with different heights at different locations in Section A-A' were modeled, the mesh for each column was not refined at the lower boundary where the column connects to the WT. If a unit is partially above and partially below the WT, then the node at that elevation, regardless of its original grid size, was shortened and connected to the WT. This method of treating the lower boundary does not introduce numerical mesh effects in one-dimensional runs. One-dimensional columns also optimize solution controls, namely the maximum time allowed and the desired accuracy in pressure head changes. Different solutions were tested using content and variable nodal time constants. Most of these exercises are important for evaluating the accuracy of numerical simulation but are not crucial to understanding the physical behavior of partially saturated systems. The only results of these numerical exercises that will be briefly mentioned are the conductivity weighting effects. Figure 3 includes a comparison of two runs: one that used the harmonic mean to evaluate the effective conductivity between two neighboring nodes and one that used upstream (higher potential) conductivity to evaluate fluxes. Lack of a noticable difference between the two coarse grid runs indicated that the conductivity weighting effect is not a major source of numerical uncertainty in steady-state simulations.

The results of a 0.1- and 0.5-mm/yr flux in the nonwelded units are compared in Figure 4. The net infiltration at Yucca Mountain is estimated at 0.1 to 0.5 mm/yr (Montazer et al., 1985; Peters et al., 1986b; DOE, 1986). Figure 4 shows that nearly all of the units at Yucca Mountain are saturated if the infiltration is 0.5 mm/yr. At 0.1-mm/yr infiltration, the calculated saturation in the TSw unit is one standard deviation higher than the mean ambient saturation (the RIB ambient saturation value is 0.65 $\pm$0.19). The calculated saturation of the thick Topopah Spring Member has been determined by characteristic curves. If an unsaturated unit is thick enough to damp the boundary effects, it will have a stable range of constant pressure and zero pressure gradient, and the flow will be driven by the gravity gradient and the partially saturated conductivity exactly matching the infiltration rate. If we want to match calculated results with field observations for a vertical column, we can adjust either the infiltration rate or the conductivity value (saturated conductivity and/or characteristic curve parameters).

In this study, we did not adjust the Topopah Spring saturation value, which according to field observation is within the range of the ambient saturation value for the 0.1-mm/yr case. However, we did try to adjust the parameters for the nonwelded units. Ambient saturation is 0.56 $\pm$0.17 for the PTn unit (Sinnock et al., 1984); 0.90 for the CHnv unit; and 0.91 $\pm$0.06 for the CHnz unit (Montazer and Wilson, 1984). Figure 4 shows that if we use characteristic curves corresponding to narrow pore size distribution as we did before we get very low saturation values for nonwelded units, especially the PTn unit. Characteristic curves corresponding to wider pore size distribution yield saturation values closer to the measured ambient saturations, at least for the PTn unit. If, for the CHnv unit, there are samples or experiments indicating a wider pore size distribution than the values in Table 2 indicate, we can also obtain closer agreement of

calculated and measured saturations for this unit. Our main reason for using different characteristic parameters for PTn and CHnv is to bring saturation values for these units higher so that we will have high conductivity values for these nonwelded units, which are leading candidates for lateral flows. With high conductivities within the range of available data, we maintain a high level of conservativeness in assessing the potential of lateral flows for removing fluid from unsaturated units.

4.0 LATERAL REDISTRIBUTION

The main reason for using fine mesh near interfaces in one-dimensional vertical column models is the possible presence of large variations in saturation, pressure, and potential as water moves vertically from one unit to another that has very different material properties. The external driving force in the vertical column is gravity itself. Along the lateral direction in the two-dimensional models, there is only one interface: the formation-fault boundary. Furthermore, the external driving force is much weaker, namely the lateral component of gravity. For a 6° tilting, the sine of 6° is 0.1. So the external driving force along the lateral direction is approximately 10% of gravity. If the movement of partially saturated flow is determined by the balance of external force with internal capillary forces, the weaker external force also requires less capillary force to readjust and to balance the external force. Based on this argument, we may expect smaller lateral than vertical variation in saturation, capillary pressure head, and potential.

Table 5 and Figure 5 summarize the five meshes used in the two-dimensional studies. The first three meshes were used to evaluate lateral mesh refining effects. Because the digitized grid of Section A-A' has a column-column separation of 76.2 m (250 ft), the first two-dimensional model is constructed with three columns; the first column next to the GDF is 38.1 m wide, and the next two columns are each 76.2 m wide and are attached to the western side of the first column. The total lateral extent of the three-column model is 190.5 m [38.1 + (2 x 76.2 m)]. The seepage boundary nodes that are connected to fixed potential nodes at atmospheric pressure (zero pressure head) are on the eastern side of the first column. The seepage nodes have the same elevations as the GDF column. The first column has the same vertical grid as the seepage nodes, with each node at $\Delta x \cdot \tan(6°)$ higher, where $\Delta x = 19.05$ m. The second column is higher than the first by $57.15 \cdot \tan(6°)$ m, and the third column is an additional $76.2 \cdot \tan(6°)$ m higher. Meshes in Figure 5 include nodes above and below the WT. In the simulations the nodes below the WT have been discarded. The height of the node just above the WT in each column has been adjusted, and the node has been connected to the zero-pressure WT boundary.

To check whether the lateral grid with $\Delta x = 76.2$ m is too wide, we refine the mesh in two ways. In one refinement we evenly reduce the width fourfold so that the grid size is $\Delta x = 19.05$ m, and the total width is modeled by ten columns. In the second refinement, we use a nonuniform grid with the first column 0.6 m wide, the second column 1.2 m wide, and subsequent columns approximately doubled in width until the width reaches

76.2 m. The total width of the ten-even-column mesh and the nine-nonuniform-column mesh is the same as the three-column coarse mesh (190.5 m).

The fourth and fifth meshes in Figure 5 and Table 5 cover wider sections. The five-column model adds two more columns, each 76.2 m wide, to the west side of the three-column model to extend the total width to 343 m. The nine-column model further extends the section to 648 m wide with four additional 76.2-m-wide columns. These wider models have been used to study the effects of larger sections on the distribution of fluid flow in a tilted, layered system under partially saturated conditions.

The results for the first three 190.5-m-wide models with 0.1-mm/yr infiltration are given in Figures 6 through 14, and the results for wider section models are given in Figures 15 and 20. For each model, saturation, pressure head, potential, conductivity, darcy velocity, and matrix velocity distributions are plotted. For saturation, pressure head, and potential, both vertical profiles along each column and cross-section contours over the modeled region are plotted to illustrate two-dimensional distributions. Vertical profiles are plotted from calculated results without interpolations. Vertical profile plots can also illustrate clearly deviations of the two-dimensional results from the one-dimensional results. On the other hand, profile plots can be unwieldy when there are many columns and when profiles are very close to each other. Contour plots illustrate the two-dimensional effects better than profile plots. However, contour plotting results are sensitive to spline-fitting interpolation and extrapolation schemes. In alternating layer systems with discontinuous saturation changes and abrupt pressure and potential slope changes across interfaces between different welded and nonwelded units, contour distortions caused by spline-fitting can be large near the interfaces. It is important to recognize these distortions in analyzing contour results. Profile and contour plots are given to complement each other.

Six profile plots and three contour plots are presented for each model. The conclusions that can be drawn from the results for the five models are essentially the same. It is, therefore, easier to analyze the results of simple models first before checking the results of complex models. For the three-column model, Figure 6a shows that the matrix saturation along Column 1 closest to the GDF boundary is slightly higher than the saturation of the other two columns. The eastern tilting of the units results in slightly higher matrix saturations on the eastern side of the cross section. To illustrate this small saturation redistribution, a 1% saturation interval was used to plot contours of the area bounded by Column 1 and Column 3 in Figure 7a. The contours are labeled in 2% divisions with the label in the middle of the contour corresponding to 86%. Using a 1% interval many contours have been plotted near the welded-nonwelded interfaces because saturations change discontinuously across these interfaces. The distortions are also large. The contours are for the matrix saturation distributions. In Figure 6a profiles of fracture saturations are also plotted. The fractures are dry except at the lowest nodes connected to the WT.

Figures 6b and 7b show that the pressure head along Column 1 closest to the seepage boundary is slightly higher than pressure heads of the other

two columns. Pressure head values remain negative, and deviations of two-dimensional three-column results from one-dimensional one-column results (Figure 3b) are small. Deviations of two-dimensional potential distributions (Figures 6c and 7c) from one-dimensional potential distributions (Figure 3c) are even smaller. From matrix saturation, pressure head, and potential results of the three-column model, tilting of the units changes the vertical distributions very little.

Figure 8a illustrates conductivity distributions in the three-column model. Conductivity times potential gradient determines darcy flux. Figure 8b shows that vertical darcy velocity along Column 1, closest to the GDF boundary, is approximately 10% higher than the 0.1-mm/yr infiltration rate; flow in Column 2, in the middle, is approximately 0.1 mm/yr; and flow in Column 3, away from the GDF boundary, is approximately 10% lower than 0.1 mm/yr. In Figure 8b lateral components of darcy velocity from Column 3 to Column 2 and from Column 2 to Column 1 are also plotted. In the slanted meshes used in this study, lateral fluxes between two neighboring columns are evaluated for both pressure and elevation differences of neighboring nodes. Because elevation differences are included in flux calculations, a lateral velocity is not a horizontal velocity. Lateral velocities measure flux magnitudes along layers parallel to tilted interfaces. In Figure 8b lateral components are plotted on the same scale as vertical components. Figure 8b mainly shows that lateral darcy velocities are much smaller than vertical darcy velocities. Details of lateral flow distributions of the nonwelded PTn unit will be plotted later in a different fashion after the results of other models are discussed.

Groundwater velocity through pores can be determined from darcy velocity, saturation, and porosity. The matrix velocity profiles of the three-column model are shown in Figure 8c. Discontinuity of matrix pore velocity across interfaces originates from different porosity values in different layers. For example, because the upper lithophysae-rich TSw1 unit has a higher porosity value than the lower TSw2 unit, the corresponding matrix pore velocity changes from low values in TSw1 to high values in TSw2. All other quantities (saturation, pressure, potential, conductivity, and darcy velocity) are the same in TSw1 and TSw2, which have the same partially saturated characteristic curves. Based on matrix pore velocity, we can calculate nondispersive groundwater travel time from the repository to the WT. Groundwater travel time based on vertical velocity along Column 1 is approximately 20% greater than the groundwater travel time along Column 3.

Figures 9 through 14 are the results for the ten-even-column model and for the nine-nonuniform-column model, respectively. The sequence and the content of the profile and contour subplots for each model are the same as the three-column model. With finer lateral grids, saturation contour plots in Figures 9a and 12a are visually smoother than the three-column plot in Figure 6a. Visual differences are due mainly to spline-fitting distortions. Calculated results at nodes are not that sensitive to mesh refinements. We will analyze mesh refinement effects more quantitatively later, in comparative plots. Because the contour plots cover only the region between the easternmost and the westernmost columns, the contour plot for the ten-even-column model covers a slightly larger section than the nine-nonuniform-column model and the three-column model. Scanning through the

subplots in saturation, pressure head, potential, conductivity, darcy velocity, and matrix velocity in Figures 9 through 14, we observe the same mild redistribution effects with higher saturation, pressure head, potential, conductivity, darcy velocity, and matrix velocity values along the eastern columns than along the western columns. Results in Figures 6 through 14 indicate that the three-coarse-column mesh is adequate to model the lateral variations of the fluid flow field for the tilted interfaces bounded by a seepage boundary in the 0.1-mm/yr infiltration cases. The only noticeable differences among the results of these three models with different mesh refinements are the velocities at the very bottom, where the columns are connected to the WT. The onset of fracture flow near the WT is resolved in more detail with the finer mesh models. Above the WT, flow remains in the matrix everywhere for the 0.1-mm/yr infiltration.

Because a three-column mesh with Δx = 76.2 m can be used to model lateral variations of the fluid flow field of a 190.5-m tilted section, we added two and six more columns to the west side of the three-column mesh. Figures 15 through 20 show the results for the five-column, 343-m-section model and the nine-column, 648-m-section model, respectively. With wider cross sections, lateral variations in saturation, pressure head, potential, conductivity, darcy velocity, and matrix velocity are proportionally larger. With more columns and larger vertical offsets, profile plots of wider section models are more complex than profile plots of the early three-column, 190.5-m-section model. It is more illuminating to compare the contour plots in Figures 15 through 20 with corresponding ones in Figure 6. Saturation and pressure head contours illustrate fluid flow redistribution effects with higher saturation and pressure head in the east than in the west. Potential contours also show an interesting reorientation effect. In a 190.5-m section with three columns, equal potential lines are approximately parallel to tilted interfaces as shown in Figure 7c. In a 343-m section with five columns, equal potential lines become more horizontal and less parallel to the tilted interfaces as shown in Figure 16c. And in a 648-m section with nine columns, equal potential lines are even more horizontal in the midsection, away from the eastern and western boundaries as shown in Figure 19c. This indicates that the direction of the fluid flow is nearly vertical in the interior of wide sections with tilted alternating layers. The width of Section A-A' between GDF and SC is 1,266.5 m.

The results of the five models with a 0.1-mm/yr infiltration are summarized and compared in Figure 21. Matrix saturation, pressure head, potential, conductivity, vertical darcy velocity, and vertical matrix velocity for nodes in the middle of the TSw2 unit are plotted versus the horizontal coordinate. From the results of the first three models with three columns, ten-even columns, and nine-nonuniform columns for a 190.5-m section, we note that numerical uncertainties associated with lateral mesh refinements are small. Based on the differences between saturation for the easternmost and westernmost columns, the rate of linear saturation change is calculated at 17%/km for the 190.5-m models. Lateral profiles of the five-column, 343-m-section model are approximately linear as are those of the 190.5-m-section models. The difference between the saturation in Column 1 and the saturation in Column 5 is 4.4% which is equivalent to 15%/km. For the nine-column, 648-m-section model, lateral profiles have

a slight sigmoid (s-shaped) flexure, with more variation near the side boundaries and less variation toward the middle of the section. The difference between the matrix saturation in Column 1 and in Column 9 is 6% which is equivalent to 10%/km. We expect that lateral distributions from even wider section models will be more sigmoidal, with variations in saturation in the interior of the sections away from the side boundaries even less than 10%/km. The 10% saturation-change/kilometer rate is probably high for sections wider than 648 m. Based on the results of the nine-column, 648-m-section model, upper bounds can also be estimated for the other variables: pressure head, 60 m/km; potential, 44 m/km; vertical darcy velocity, 0.085 mm/yr/km; and vertical matrix pore velocity, 0.79 mm/yr/km.

The time for groundwater to travel from the repository to the WT can be calculated from the vertical matrix pore velocity. For the nine-column model, groundwater travel time along the easternmost column is approximately 50% less than travel time along the westernmost column. If the section width is doubled, groundwater travel time from different points in the repository is expected to vary by a factor of 2. Fluid flow redistribution induced by tilting units is unlikely to introduce order-of-magnitude changes in the groundwater travel time for the 0.1-mm/yr infiltration cases.

In the potential lateral distribution shown in Figure 21c, we also plot the elevation of the midplane of the TSw unit, which has an equivalent elevation variation of 105 m/km associated with the 6° tilting. Because the midplane of a unit is parallel to tilted interfaces, the lateral profiles in Figure 21 are along the direction with the dip angle of 6°. Along the tilted midplane, potential is higher in the west than in the east. If we follow a horizontal direction with constant elevation, potential is higher in the east than in the west. In a horizontal direction with constant elevation, the fluid flow is driven by the pressure field, which is higher in the east than in the west. Overall flow direction is more clearly inferred in potential contour plots (Figures 7c, 16c, and 19c) that show nearly horizontal equal potential lines quasi-parallel to the tilted interfaces. Overall flow direction is nearly vertical, with a small component toward the west. In analyzing lateral flow along a tilted layer, it is important to recognize the overall flow direction.

In the vertical profile plots of darcy velocity and matrix velocity (Figures 8b, 17b, and 20b), both vertical velocities along the columns and lateral velocities from column to column are included. Comparison shows that the magnitude of the lateral velocities is much smaller than the magnitude of the vertical velocities. The magnitude of lateral flows in the PTn unit is greater than the magnitude, in other units. Figure 22 illustrates column-to-column lateral darcy velocities versus the horizontal coordinate for this unit. Lateral flow is the mechanism to redistribute vertical infiltration by channeling water from the west to the east, so that the vertical darcy flux is higher in the east than in the west, and saturation is higher in the east than in the west. Magnitudes of lateral flow are higher in the middle of the cross section than near the side boundaries. For the 0.1-mm/yr cases in Figure 22, lateral flows are zero, $x = 0$, at the seepage boundary. In other words, water does not exit through the fault-formation boundary. The lateral gravity gradient associated with the tilting of the interfaces cannot overcome the capillary forces that hold water in partially saturated formations.

The onset of seepage flows is simulated in the 0.5-mm/yr infiltration cases. Figures 23 through 28 give the results for the three-column, 190.5-m-section model and the five-column, 343-m-section model, respectively. Based on the one-dimensional results (Figure 4), the units are nearly saturated in the 0.5-mm/yr infiltration cases. Figure 4b shows that the pressure value at the interface between the CHnv unit and the CHnz unit is nearly zero. In the three-column, 190.5-m-section model for the 0.5-mm/yr infiltration case, seepage flow is observed only at the CHnv-CHnz interface (Figure 25b). It is of interest to note that in this case, seepage flow is still matrix flow. The fractures at the exit point are noticeably saturated (Figure 23a) but still below the phase constriction cutoff to initiate fracture flow (Wang and Narasimhan, 1985). When we use the five-column, 343-m-section model for the 0.5-mm/yr infiltration case, the wider section allows more saturation and pressure redistribution. The onset of fracture flow (Figure 28d) and seepage velocity (Figure 28b in log scale) is much greater than in the three-column model (Figure 25b). However, in terms of mass fluxes, both the three-column and five-column models yield approximately the same 8% lateral diversion. In other words, 8% of the infiltration on the GRD exits at the CHnv-Chnz interface in the two-dimensional section, and the remaining 92% moves down to the WT. The total water introduced into the cross section is proportional to the infiltration rate times east-west width on the GRD. In a wider section, more water enters the cross section on the GRD, and proportionally more water leaves the cross section at the side seepage point. If the amount of water flux driven by the lateral gravity gradient parallel to the tilted interfaces is larger than the matrix saturated conductivity, fracture flows will be initiated. For wide sections with seepage flow through fractures, the velocity of the fracture flow will be orders of magnitude larger than the matrix velocity. Based on the material properties used in this study, seepage flow is observed only in the CHnv-Chnz interface for the 0.5-mm/yr cases. If different characteristic curves are used for the units, we may also generate results with seepage flow in other units, provided the units have pressure values of nearly zero and the redistribution effects are strong enough to increase pressure values to nonnegative ranges. Based on the material properties used in this study, the saturation and pressure distributions for the 0.5-mm/yr infiltration do not represent ambient partially saturated conditions at Yucca Mountain. Therefore, predictions of the existence of seepage flows in the 0.5-mm/yr cases are mainly modeling exercises.

5.0 SUMMARY AND DISCUSSION

In modeling the hydrology of Yucca Mountain, it is important to assess the impacts of faults that traverse the alternating layers. First, if faults are barriers to fluid flows, these faults will partition the system into separate hydrologic blocks, and we can focus on studying the flows through the interior of the blocks. Second, if the faults are the main conduits for fluid flow, we should focus on studying the fault flows. In saturated systems, there is a clear distinction between these two possibilities. A closed fault is treated as a no-flow boundary, and an open fault may be treated as a constant potential boundary. In the latter case, faults may help transport water from a far-removed source or may help

remove water to a deeper sink. In partially saturated systems, there is not as clear a distinction between an open and a closed fault.

If a fault is made up of broken-up mass because of brecciation, it will have very coarse openings that can be easily drained. If the openings are dry, there is no fluid to be transported. On the other hand, a dry opening is not a barrier to fluid flow. If water enters the opening, the opening will be highly permeable and offer low resistance to fluid movement. Under partially saturated conditions, an open fault becomes a passive boundary that can transport water if water enters it but cannot hold water because the capillary force in large openings is very weak.

If a fault is sealed with gouge and fine-grained materials, it can hold water and may even attract water with the strong capillary force associated with small openings. On the other hand, small openings have low permeability and cannot be good conduits for transporting fluid. Under partially saturated conditions, a closed fault becomes a relatively wet zone that passively keeps water in nearly static conditions.

There is a third, remote, possibility that the fault may have a unique combination of saturated and unsaturated characteristics. If the fault material can maintain both strong capillary attractive force and large permeability, then the fault can pull water away from the formation and transport it quickly away from the system. We cannot rule out the existence of such a unique combination wherein fault flow would control the partially saturated hydrology. Because basic rock compositions in the fault will likely be altered tuff also, tuff hydrologic parameters from several previous reports in Appendix A are compiled and compared to check whether material properties for a fault with a high saturated conductivity and strong suction characteristics can be used. There are no data for the fault zone materials to clearly distinguish whether faults in tuff formations have open, closed, or exotic characteristics.

In this study, we do not use material properties to represent the fault. We treat the fault-formation boundary as a seepage boundary and assume that the fault is so open that the capillary force is zero and the saturated permeability is infinite. The face of the fault behaves like the surface of a hillside exposed to atmospheric pressure. We focus, therefore, on the interior of the formation to determine whether water can overcome the capillary forces holding it inside the tuff matrix. If water does not exit through the fault-formation boundary, the seepage boundary is essentially a closed boundary. If water remains inside the formations, distribution of fluid flow will be independent of whether the fault is open or closed. The only possibility we do not model in this study is the third possibility, wherein the fault acts like a strong capillary suction sink as well as a high-permeability conduit under partially saturated conditions.

Based on the results from models with two-dimensional cross sections for alternating layers tilted toward the seepage boundary on the east, we may conclude that for the 0.1-mm/yr infiltration

- Eastern tilting of the units contributes to the redistribution of flow, resulting in higher saturations and higher vertical velocities in the eastern side of a block bounded by faults. This

redistribution effect is approximately proportional to the width of the cross section.

- Nonwelded units are major channels in redistributing vertical infiltration. Lateral flow is greater in the middle of a cross section than near the side boundaries.

- Tilting itself is not a strong enough mechanism to induce drastic changes in the saturation, pressure, and potential distributions to drive flows into fault zones.

The mild lateral variations in saturation, pressure, and potential indicate that the one-dimensional results are fairly good estimates of ambient conditions. The lateral tilting mechanism is a second-order perturbation that does not globally change the downward, gravity-driven flow patterns. So long as fluid flow remains inside partially saturated units, redistribution effects due to tilting will not introduce order-of-magnitude differences in fluid transport predictions. If the system is on the verge of making a phase transition from a partially saturated to fully saturated condition, as in the case of the 0.5-mm/yr infiltration, the lateral tilting mechanism can perturb the system and change a fraction of fluid flow from dispersed slow flows percolating through the formations to concentrated fast flows rushing down the faults. If fault flow is important, the early arrival portion of the groundwater travel time distributions may be controlled by the fault characteristics. For ambient conditions with large negative pressures in all partially saturated units, it is unlikely that the lateral tilting mechanism can perturb the pressure and saturation field significantly enough to overcome the negative capillary forces holding water in formations and to change groundwater travel time distributions drastically.

6.0 REFERENCES

Bauer, S. J., "Preliminary Report on Yucca Mountain Fracture Characteristics," Memorandum to J. R. Tillerson dated March 27, 1986, Appendix D, Attachment 1 of the "Site Characterization Plan Conceptual Design Report," SAND84-2641, compiled by H. R. MacDougal, L. W. Scully, and J. R. Tillerson, Sandia National Laboratories, Albuquerque, NM, 1987.

Brooks, R. H., and A. T. Corey, "Properties of Porous Media Affecting Fluid Flow," J. Irrig. Drain. Div., Am. Soc. Civil Eng., 92(IR2), 1966, pp. 61-88.

Burdine, N. T., "Relative Permeability Calculations from Pore-Size Distribution Data," Petr. Trans., Am. Inst. Mining Metall. Eng., 198, 1953, pp. 71-77.

DOE (U.S. Department of Energy), "Nuclear Waste Policy Act Environmental Assessment of the Nevada Nuclear Waste Storage Investigations (NNWSI) Project," 1986.

Harrold, A., C. C. Barton, and P. Montazer, "Statistical Analysis of Fracture Roughness Profiles in Volcanic Tuffs, Yucca Mountain, Nevada," EOS, 66(46), 1985, p. A83.

Klavetter, E. A., and R. R. Peters, "Estimation of Hydrologic Properties of an Unsaturated, Fractured Rock Mass," SAND84-2642, Sandia National Laboratories, Albuquerque, NM, 1986, 55 pp.

Montazer, P., and W. E. Wilson, "Conceptual Hydrologic Model of Flow in the Unsaturated Zone, Yucca Mountain, Nevada," USGS-WRI-84-4345, U.S. Geological Survey, Lakewood, CO, 1984, 55 pp.

Montazer, P., E. P. Weeks, F. Thamir, S. N. Yard, and P. B. Hofrichter, "Monitoring the Vadose Zone in Fractured Tuff, Yucca Mountain, Nevada," Proceedings, National Water Well Association Conference on Characterization and Monitoring of the Vadose (Unsaturated) Zone, Denver, CO, November 19-21, 1985.

Mualem, Y., "A New Model for Predicting the Hydraulic Conductivity of Unsaturated Porous Medium," Water Resour. Res., 12, 1976, pp. 513-522.

Narasimhan, T. N., P. A. Witherspoon, and A. L. Edwards, "Numerical Model for Saturated-Unsaturated Flow in Deformable Porous Media," Part 2, the Algorithm, Water Resour. Res., 14, 1978, pp. 255-261.

Narasimhan, T. N., M. Alavi, and T. Tokunaga, "COVE2A Benchmarking Studies," Memorandum to W. Prindle and N. Hayden, Lawrence Berkeley Laboratory, Berkeley, CA, 1985.

Nimick, F. B., S. J. Bauer, and J. R. Tillerson, "Recommended Matrix and Rock-Matrix Bulk, Mechanical and Thermal Properties for Thermomechanical Stratigraphy of Yucca Mountain," Appendix O of the "Site Characterization Plan-Conceptual Design Report," SAND84-2641, compiled by H. R. MacDougall, L. W. Scully, and J. R. Tillerson, Sandia National Laboratories, Albuquerque, NM, 1984.

Ortiz, T. S., R. L. Williams, F. B. Nimick, B. C. Whittet, and D. L. South, "A Three-Dimensional Model of Reference Thermal/Mechanical and Hydrological Stratigraphy at Yucca Mountain, Southern Nevada," SAND84-1076, Sandia National Laboratories, Albuquerque, NM, 1984.

Peters, R. R., E. A. Klavetter, I. J. Hall, S. C. Blair, P. R. Heller, and G. W. Gee, "Fracture and Matrix Hydrologic Characteristics of Tuffaceous Materials from Yucca Mountain, Nye County, Nevada," SAND84-1471, Sandia National Laboratories, Albuquerque, NM, 1984, 188 pp.

Peters, R. R., E. A. Klavetter, J. T. George, and J. H. Gauthier, "Measuring and Modeling Water Imbibition into Tuff," EOS, 67(44), 1986a, p. 963.

Peters, R. R., J. H. Gauthier, and A. L. Dudley, "The Effect of Percolation Rate on Water-Travel Time in Deep, Partially Saturated Zones," SAND85-0854, Sandia National Laboratories, Albuquerque, NM, 1986b.

Rulon, J., G. S. Bodvarsson, and P. Montazer, "Preliminary Numerical Simulations of Groundwater Flow in Unsaturated Zone, Yucca Mountain, Nevada," LBL-20553, Lawrence Berkeley Laboratory, Berkeley, CA, 1986.

Scott, R. B., and J. Bonk, "Preliminary Geologic Map of Yucca Mountain with Geologic Sections, Nye County, Nevada," USGS-OFR-84-494, U.S. Geological Survey, Denver, CO, 1984.

Sinnock, S., Y. T. Lin, and J. P. Brannen, "Preliminary Bounds on Expected, Postclosure Performance of Yucca Mountain Repository Site, Southern Nevada," SAND84-1492, Sandia National Laboratories, Albuquerque, NM, 1984.

SNL (Sandia National Laboratories), Interactive Graphics Information Services, NNWSI Product Numbers CAL0115 and CAL0119.

Spengler, R. W., and M. P. Chornack, "Stratigraphic and Structural Characteristics of Volcanic Rocks in Core Hole USW-G4, Yucca Mountain, Nye County, Nevada, with Geophysical Logs by D. C. Muller and J. E. Kibler," USGS-OFR-84-789, U.S. Geological Survey, Denver, CO, 1984.

Thordarson, W., "Geohydrologic Data and Test Results from Well J-13, Nevada Test Site, Nye County, Nevada," USGS-WRI-83-4171, U.S. Geological Survey, Denver, CO, 1983.

van Genuchten, M. T., "A Closed-Form Equation for Predicting Hydraulic Conductivity of Unsaturated Soils," Soil Sci. Soc. Am. J., 44, 1980, pp. 892-898.

Wang, J. S. Y., and T. N. Narasimhan, "Hydrologic Mechanisms Governing Fluid Flow in Partially Saturated, Fractured, Porous Tuff at Yucca Mountain," SAND84-7202, Sandia National Laboratories, Albuquerque, NM, LBL-18473, Lawrence Berkeley Laboratory, Berkeley, CA, Water Resour. Res., 21, 1985, pp. 1861-1874.

Wang, J. S. Y., and T. N. Narasimhan, "Hydrologic Mechanisms Governing Partially Saturated Fluid Flow in Fractured Welded Units and Porous Nonwelded Units at Yucca Mountain," SAND86-7114, Sandia National Laboratories, Albuquerque, NM, LBL-21022, Lawrence Berkeley Laboratory, Berkeley, CA, 1986, 74 pp.

Winograd, I. J., and W. Thordarson, "Hydrogeologic and Hydrochemical Framework, South Central Great Basin, Nevada-California, with Special Reference to the Nevada Test Site," USGS-PP-712-C, 1975, pp. C1-126.

TABLE 1

FORMATION THICKNESS

Unit	Thickness (m)	Elevation (m)	Tilting Angle
Tiva Canyon Welded Unit (TCw)	41.46	511.32	5.4°
Paintbrush Nonwelded Unit (PTn)	41.20	470.12	5.3°
Topopah Spring Welded, Lithophysal Unit (TSwl)	95.45	374.67	6.9°
Topopah Spring Welded Unit (TSw2)	232.08(1)	142.59	5.6°
Calico Hill Nonwelded, Vitric Unit (CHnv)	14.74	127.85	2.0°(2)
Calico Hill Nonwelded, Zeolitic Unit (CHnz)	108.02	19.83	6.6°
Pah Pass Welded Unit (PPw)	43.86	-24.03	7.0°(2)
Crater Flat Nonwelded Unit (CFUn)	80.09	-104.12	8.7°(2)
Bullfrog Welded Unit (BFw)	111.18	-215.30	

1. In constructing the meshes, this unit is further separated into three zones: above the repository midplane (RMP, 110.44 m), the disturbed zone (DZ, 50.71 m), and below the disturbed zone (70.93 m).
2. Not used in evaluating the average tilt angle (6°) of the interfaces.

TABLE 2

MATRIX PROPERTIES

Unit	Saturated Permeability k_s Conductivity (1) m^2(mm/yr)	Porosity(2) ϕ	van Genuchten Parameters α(4) (1/m)	n(4)	S_r(5)	Compressibility(3) (1/m)
TCw	2.55×10^{-18} (0.789)	0.114	8.21×10^{-3}	1.558	0.002	6.2×10^{-7}
PTn	2.45×10^{-15} (757.385)	0.448	3.05×10^{-2}	1.22	0.040	8.2×10^{-6}
TSw1	2.33×10^{-18} (0.722)	0.143	5.67×10^{-3}	1.798	0.091	1.2×10^{-6}
TSw2	2.33×10^{-18} (0.722)	0.1168	5.67×10^{-3}	1.798	0.091	5.8×10^{-7}
CHnv	3.46×10^{-16} (107.168)	0.3541	4.40×10^{-2}	1.496	0.0852	3.9×10^{-6}
CHnz	1.73×10^{-18} (0.535)	0.3064	3.08×10^{-3}	1.602	0.1211	2.6×10^{-6}
PPw	2.84×10^{-16} (87.742)	0.2557	1.41×10^{-2}	2.639	0.0686	1.5×10^{-6}
CFUn	6.99×10^{-17} (21.637)	0.3239	3.82×10^{-3}	1.9455	0.2282	2.4×10^{-6}
BFw	3.83×10^{-16} (118.439)	0.2391	2.025×10^{-2}	3.2025	0.0584	1.7×10^{-6}

1. TCw and PTn values taken from Sinnock et al. (1984); other values taken from the NNWSI Reference Information Base (RIB, 1986), Section 1.1.4.2.
2. TCw, PTn, and TSw1 values taken from the RIB, Section 1.3.1.2.1-4; other values calculated from data in the RIB, Sections 1.1.8.1 and 1.1.3.1-2.
3. Nimick et al. (1984).
4. From Peters et al. (1984) with sample code: TCw:G4-1, PTn:G4-2, TSw1:G4-6, TSw2:G4-6, CHnv:GU3-15, CHnz:G4-11, PPw:G4-18, CFUn:G4-19/20, BFw:G4-21/22.
5. TCw and PTn values taken from Peters et al. (1984); other values taken from the RIB, Section 1.1.3.1-2.

TABLE 3

FRACTURE PROPERTIES

Unit	Bulk Saturated Permeability Conductivity[1] m^2(mm/yr)	Fracture[2] Spacing D (m) Vertical	Horizontal	Effective Aperture b (mm) Vertical	Horizontal	Discrete Fracture Permeability k_s(m^2) Vertical	Horizontal
TCw	1.18×10^{-12} (3.65×10^{5})	0.18	0.42	0.109	01.44	9.87×10^{-10}	1.72×10^{-9}
PTn	2.42×10^{-13} (7.5×10^{4})	1.02	1.12	0.114	0.118	1.09×10^{-9}	1.15×10^{-9}
TSw1	1.18×10^{-12} (3.65×10^{5})	0.21	1.26	0.114	0.208	1.09×10^{-9}	3.59×10^{-9}
TSw2	1.18×10^{-12} (3.65×10^{5})	0.21	1.26	0.114	0.208	1.09×10^{-9}	3.59×10^{-9}
CHnv	2.42×10^{-13} (7.5×10^{4})	2.12	4.49	0.146	0.187	1.77×10^{-9}	2.91×10^{-9}
CHnz	2.42×10^{-13} (7.5×10^{4})	2.12	4.49	0.146	0.187	1.77×10^{-9}	2.91×10^{-9}
PPw	1.18×10^{-12} (3.65×10^{5})	1.49	2.73	0.219	0.268	4.01×10^{-9}	6.00×10^{-9}
CFUn	2.42×10^{-13} (7.5×10^{5})	5.07	4.49	0.195	0.187	3.16×10^{-9}	2.91×10^{-9}
BFw	1.18×10^{-12} (3.65×10^{5})	0.393	3.39	0.141	0.289	1.65×10^{-9}	6.94×10^{-9}

TABLE 3

FRACTURE PROPERTIES (concluded)

Unit	Contact[3] Cutoff Aperture b_c (mm) Vertical	Horizontal	Aperture[4] Distribution Parameter β (mm^{-1}) Vertical	Horizontal	Fracture[5] Surface Contact Area ω	Discrete[6] Fracture Compressibility (1/m)
TCw	0.010	0.014	24.8	18.8	2.8%	1.32×10^{-6}
PTn	0.027	0.028	21.7	21.1	11.8%	1.90×10^{-7}
TSw1	0.027	0.050	21.7	11.9	12%	5.60×10^{-8}
TSw2	0.027	0.050	21.7	11.9	12%	1.20×10^{-7}
CHnv	0.041	0.053	16.6	13.0	15% (no zeolite)	2.80×10^{-8}
CHnz	0.132	0.169	12.7	9.91	50% (w. zeolite)	2.80×10^{-8}
PPw	0.130	0.159	9.53	7.79	35%	1.20×10^{-7}
CFUn	0.115	0.110	10.7	11.2	35%	2.80×10^{-8}
BFw	0.083	0.170	14.9	7.24	35%	1.20×10^{-7}

1. Representative values taken from Well J-13, Thordarson (1983), and Sinnock et al. (1984).
2. Derived from the average fracture spacings and orientation data in Boreholes USW G-1, UE-25a#1, USW GU-3/G-3, USW G-4, and Bauer (1987).
3. Derived from bulk saturated permeability and fracture spacings, assuming two vertical sets and one horizontal fracture set.
4. Derived with gamma distribution from permeability and surface contact area for rough-walled fractures, Wang and Narasimhan (1985).
5. Assumed to be equal to the fraction of fracture surface coated with clay, calcite, and/or zeolite, in Borehole USW G-4, Spengler and Chornack (1984).
6. Peters et al. (1984).

TABLE 4

VERTICAL GRID

Unit	Thickness (m)	Grid Spacing (m)	
		Coarse, Even Grid	Fine, Nonuniform Grid
TCw	41.46	twenty 2.07s	0.49,0.87,1.55,2.76,4.91, 4.91,4.91,4.91,4.91,2.76, 2.76,2.76,1.55,0.87,0.49
PTn	41.20	four 10.30s	0.50,0.88,1.57,2.79,4.96, 4.96,4.96,4.96,4.96,4.96, 2.79,1.57,0.88,0.50
TSw1	95.45	four 23.86s	0.67,1.20,2.13,3.78,6.72, 11.96,21.27,21.27,11.96, 6.72,3.78,2.13,1.20,0.67
TSw2 (above RMP)	110.44	four 27.61s	0.67,1.18,2.11,3.74,6.66, 11.84,21.06,21.06,21.06, 21.06
TSw2(DZ)	50.71	two 25.35s	16.90,16.90,16.90
TSw2 (below DZ)	70.93	three 23.64s	16.71,16.71,16.71,9.40, 5.28,2.97,1.67,0.94,0.53
CHnv	14.74	one 14.74	0.64,1.13,2.01,2.01,2.01, 2.01,2.01,1.13,1.13,0.64
CHnz	108.02	eight 13.50s	0.64,1.13,2.01,3.57,6.36, 11.31,11.31,11.31,11.31, 6.36,6.36,6.36,6.36,3.57, 3.57,3.57,3.57,3.57,2.01, 2.01,1.13,0.64
PPw	43.86	six 7.31s	0.70,1.25,2.22,3.95,3.95, 3.95,3.95,3.95,3.95,3.95 3.95,3.95,2.22,1.25,0.70
CFUn	80.09		0.78,1.38,2.46,4.37,7.77 7.77,7.77,7.77,7.77,7.77, 7.77,7.77,4.37,2.46,1.38, 0.78
BFw	111.18		0.78,1.38,2.46,4.37,7.77, 7.77,7.77,7.77,7.77,7.77, 7.77,7.77,7.77,7.77,7.77, 7.77,4.37,2.46,1.38,0.78

TABLE 5

LATERAL GRID

Model	Width (m)	Grid Spacing (m)
Three-column, even	190.5	38.1,76.2,76.2
Ten-column, even	190.5	19.05,19.05,19.05,19.05, 19.05,19.05,19.05,19.05, 19.05,19.05
Nine-column, nonuniform	190.5	0.6,1.2,2.4,4.8,9.7,19.4, 38.1,38.1,76.2
Five-column, even	342.9	38.1,76.2,76.2,76.2,76.2
Nine-column, even	647.7	38.1,76.2,76.2,76.2,76.2 76.2,76.2,76.2,76.2

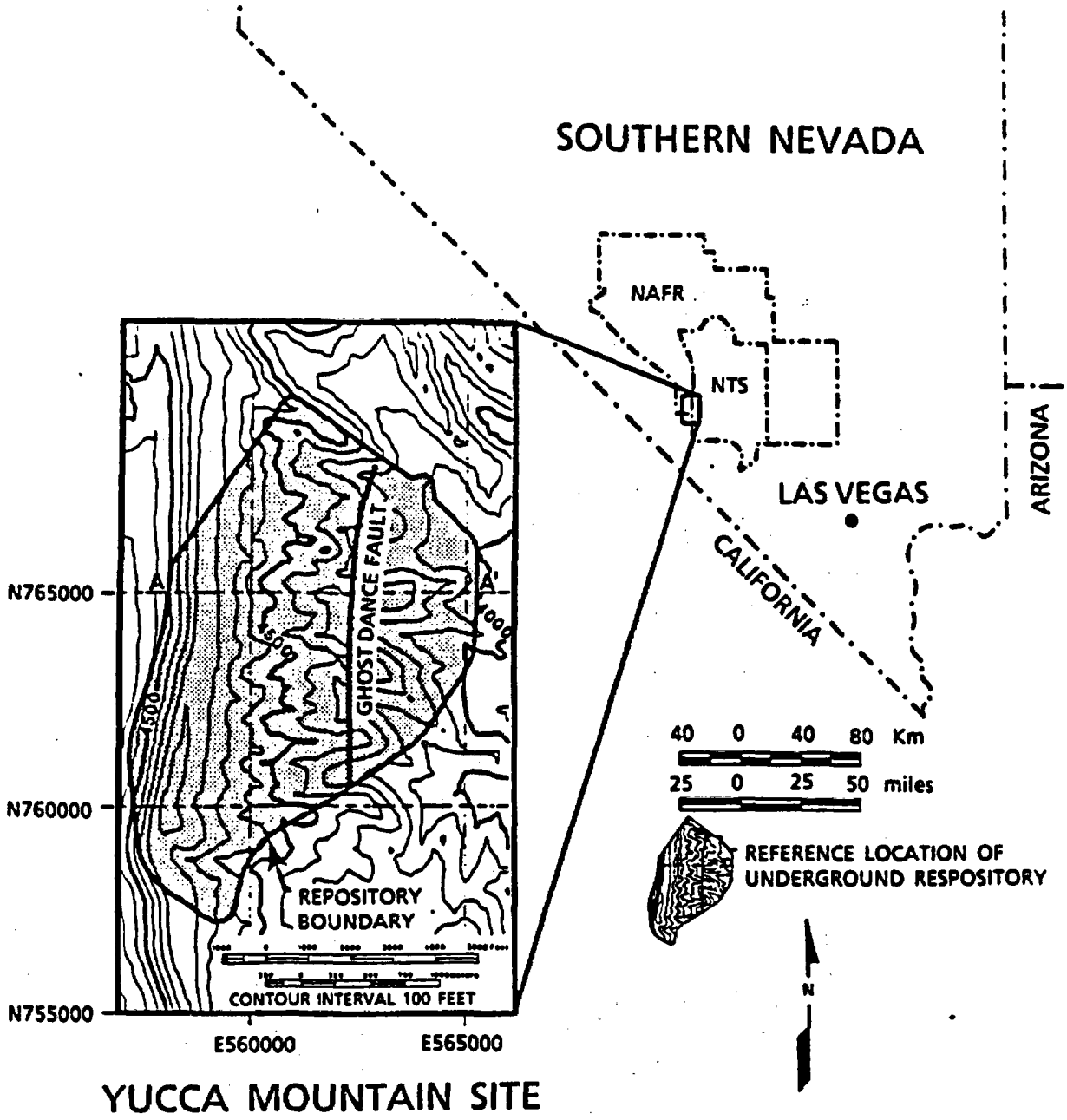

Figure 1. Location of Section A-A' Through the Central Portion of Yucca Mountain (SNL, Product CAL0119).

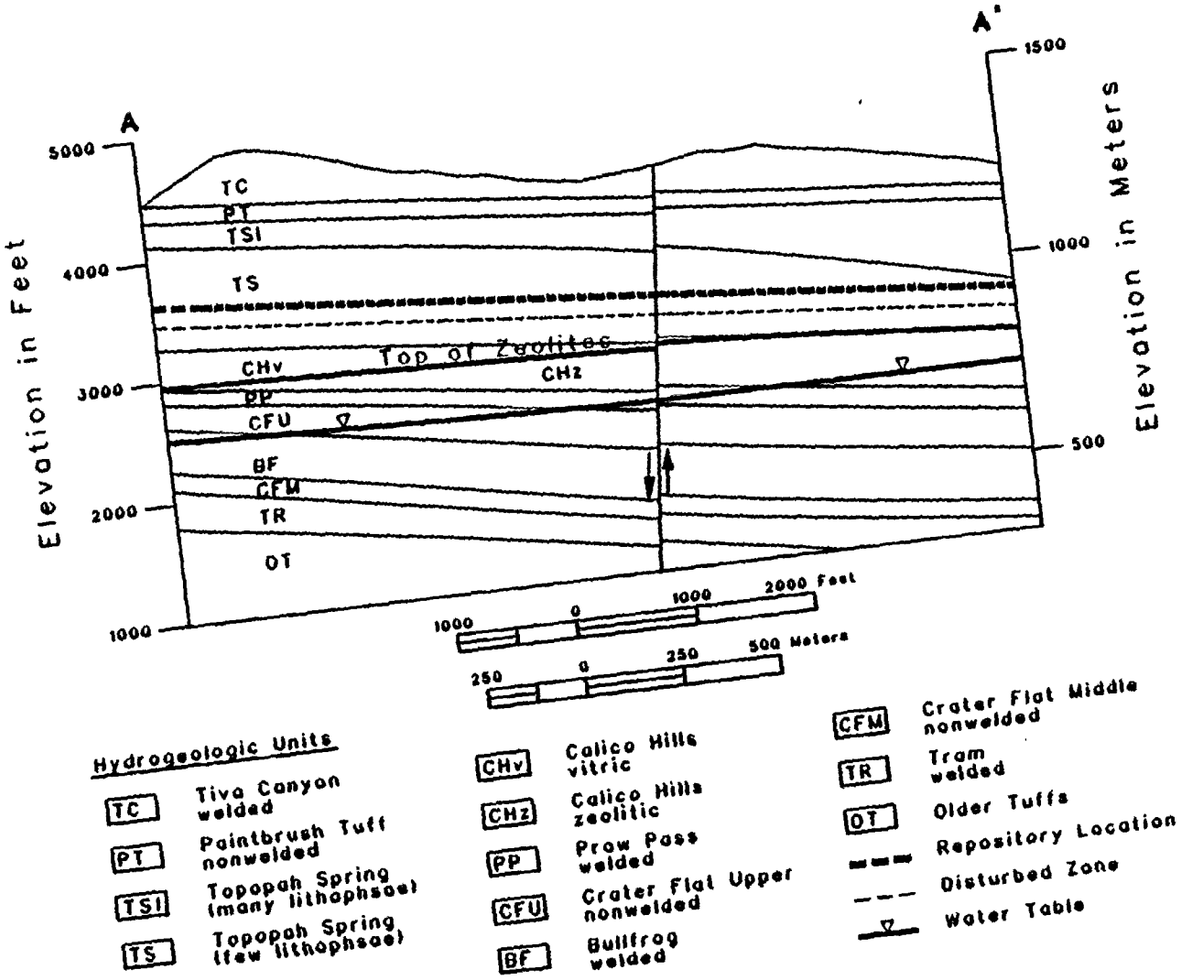

Figure 2. Hydrogeologic Cross Section A-A' at Yucca Mountain (SNL, Product CAL0115). (See Figure 1 for the Location of Section A-A'.)

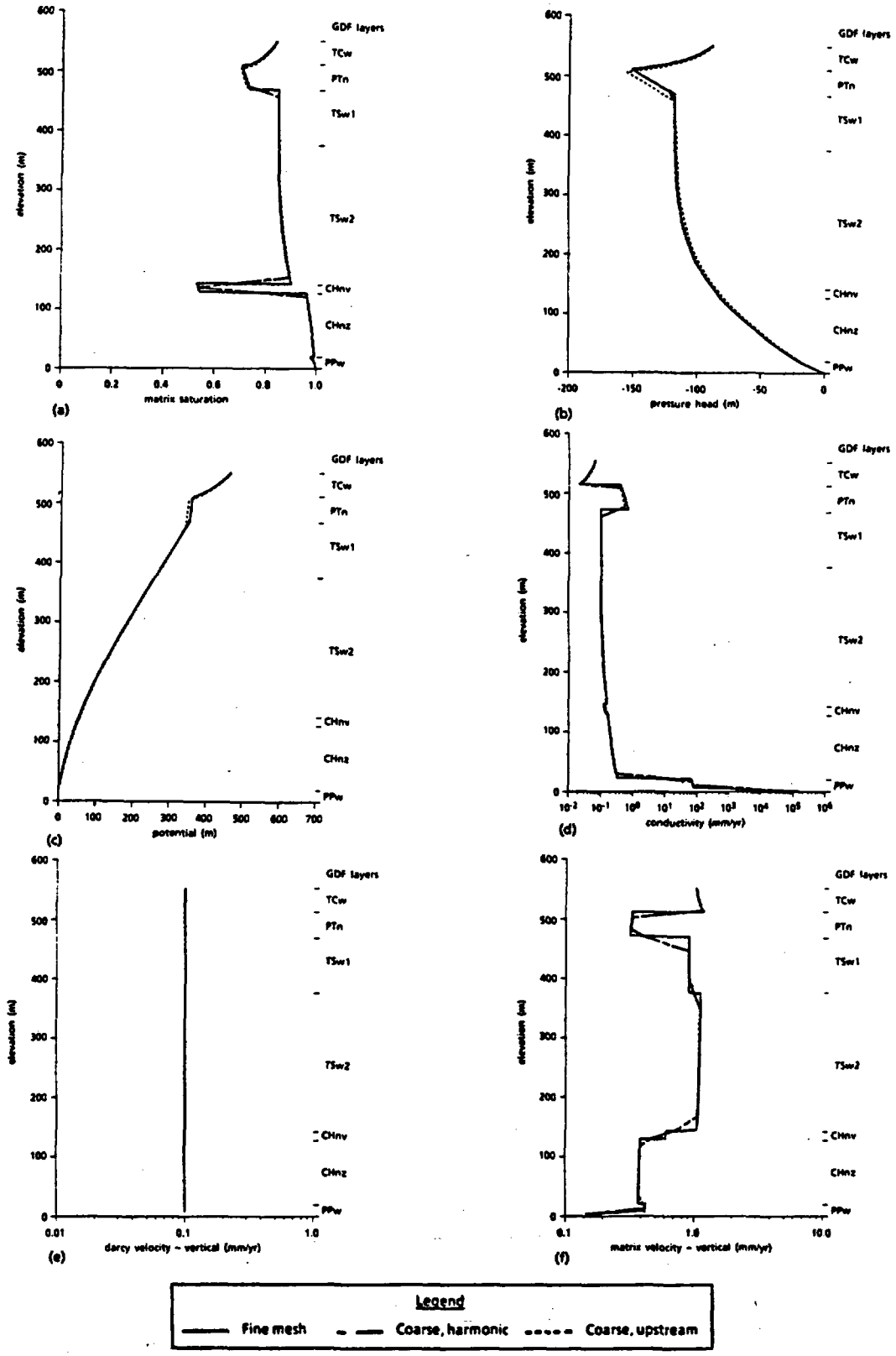

Figure 3. Plots of (a) Matrix Saturation, (b) Pressure Head, (c) Potential, (d) Hydraulic Conductivity, (e) Darcy Velocity, and (f) Matrix Velocity vs Elevation for a 0.1-mm/yr Flux for Fine and Coarse Meshes at Ghost Dance Fault.

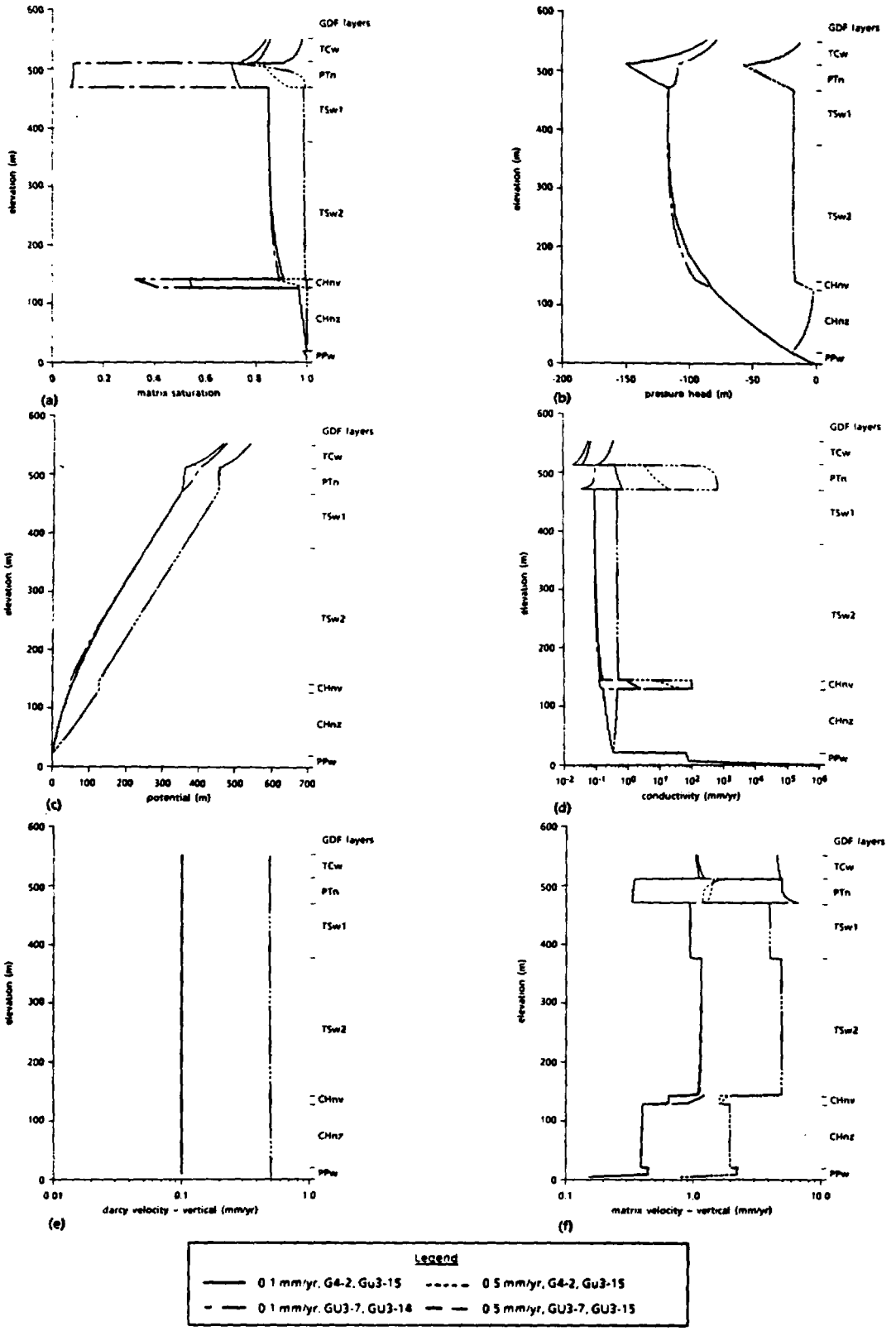

Figure 4. Plots of (a) Matrix Saturation, (b) Pressure Head, (c) Potential, (d) Hydraulic Conductivity, (e) Darcy Velocity, and (f) Matrix Velocity vs Elevation for a 0.1- and 0.5-mm/yr Flux for Different Nonwelded Tuff Properties at Ghost Dance Fault.

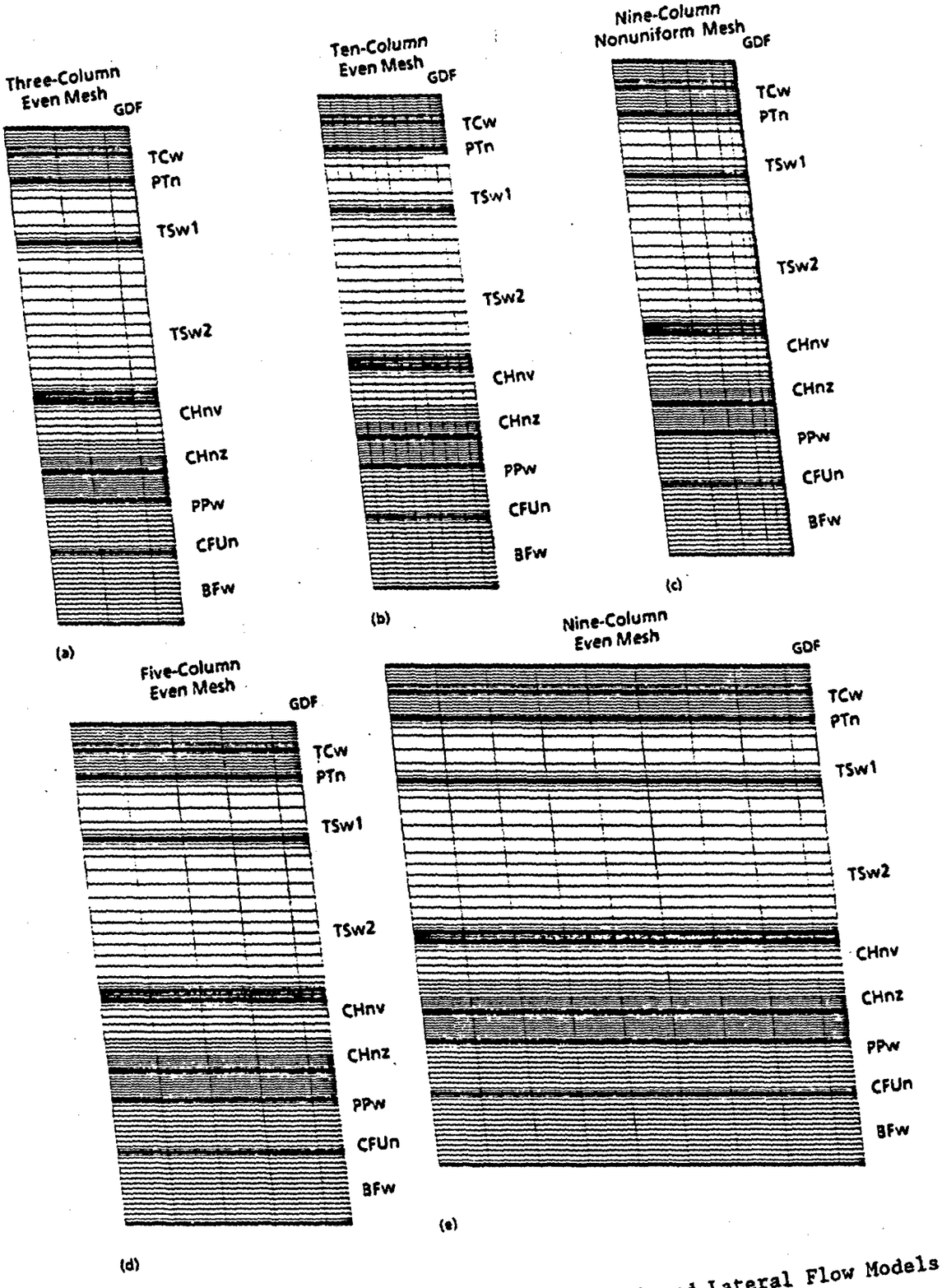

Figure 5. Two-Dimensional Grids for Vertical and Lateral Flow Models.

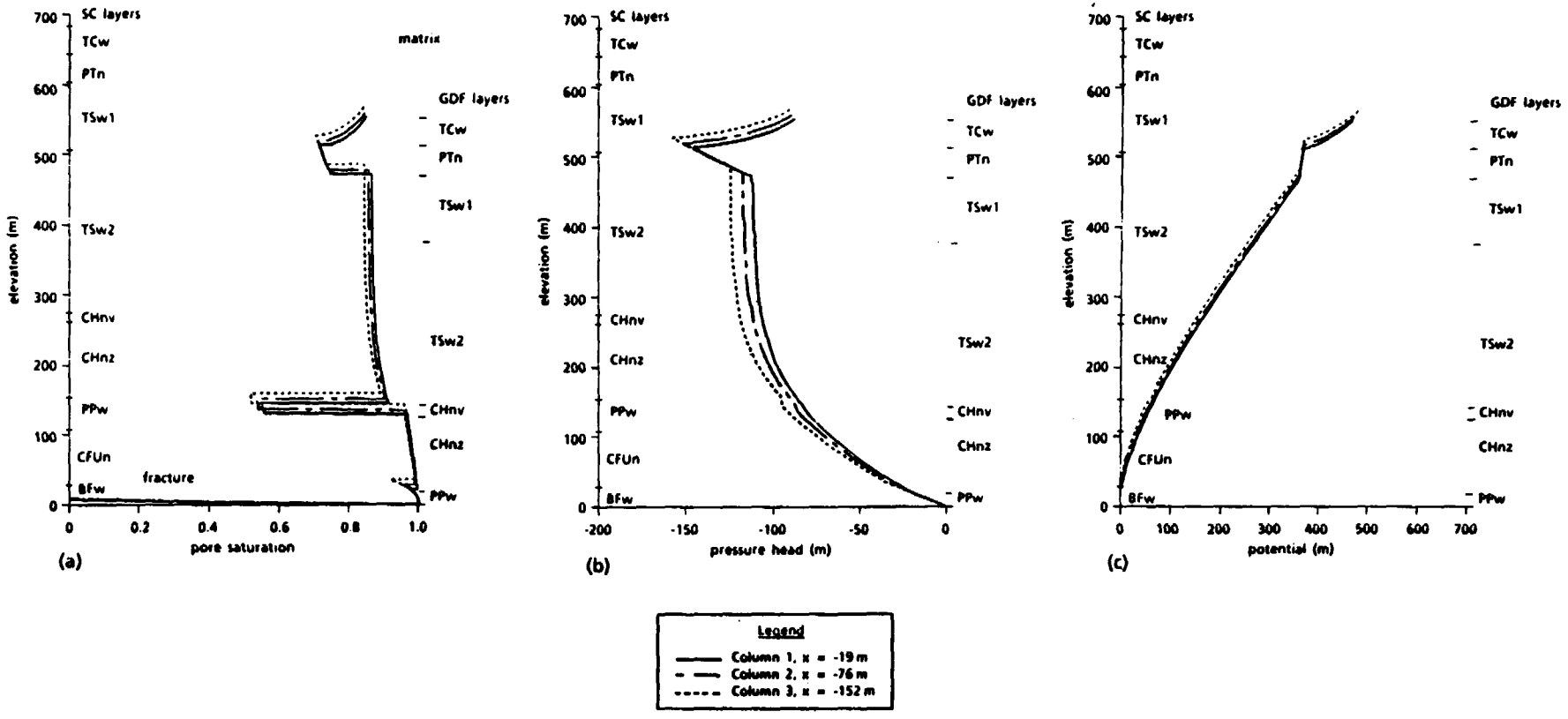

Figure 6. Plots of Elevation vs (a) Saturation, (b) Pressure Head, and (c) Potential for a 0.1-mm/yr Flux for a Three-Column (190-m) Section.

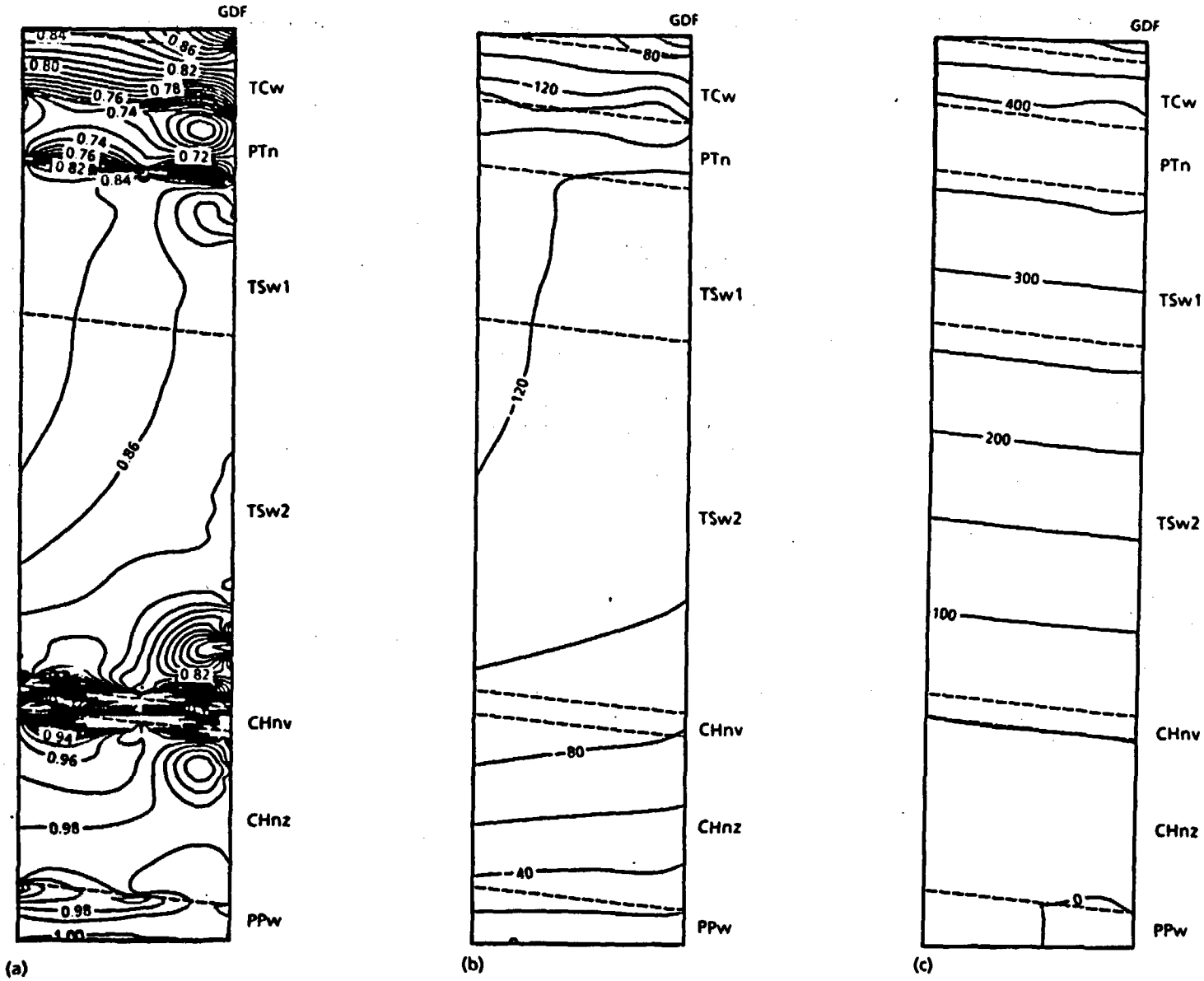

Figure 7. Contours of (a) Saturation, (b) Pressure Head, and (c) Potential for a 0.1-mm/yr Flux for a Three-Column (190-m) Section.

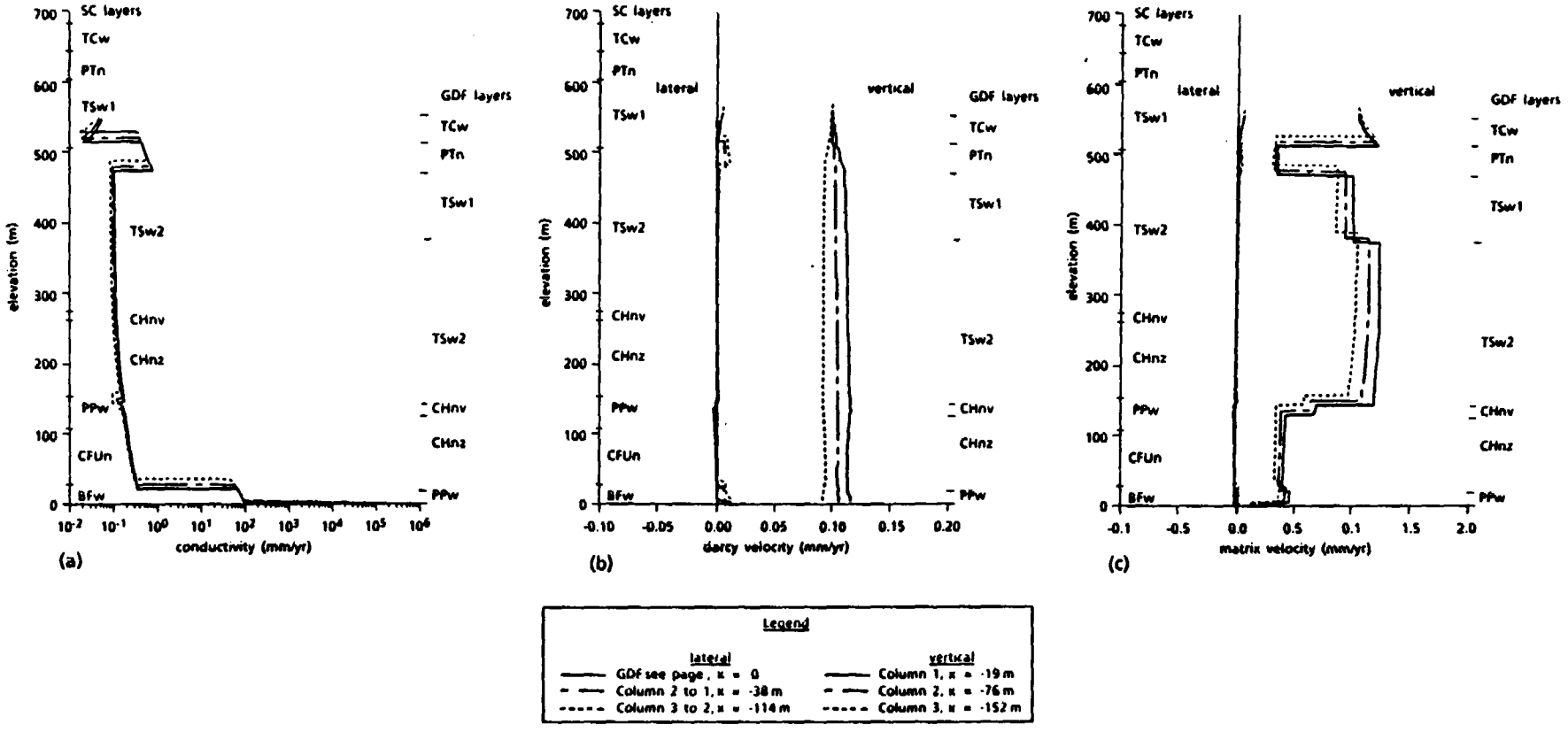

Figure 8. Plots of Elevation vs (a) Hydraulic Conductivity, (b) Darcy Velocity, and (c) Matrix Velocity for a 0.1-mm/yr Flux for a Three-Column (190-m) Section.

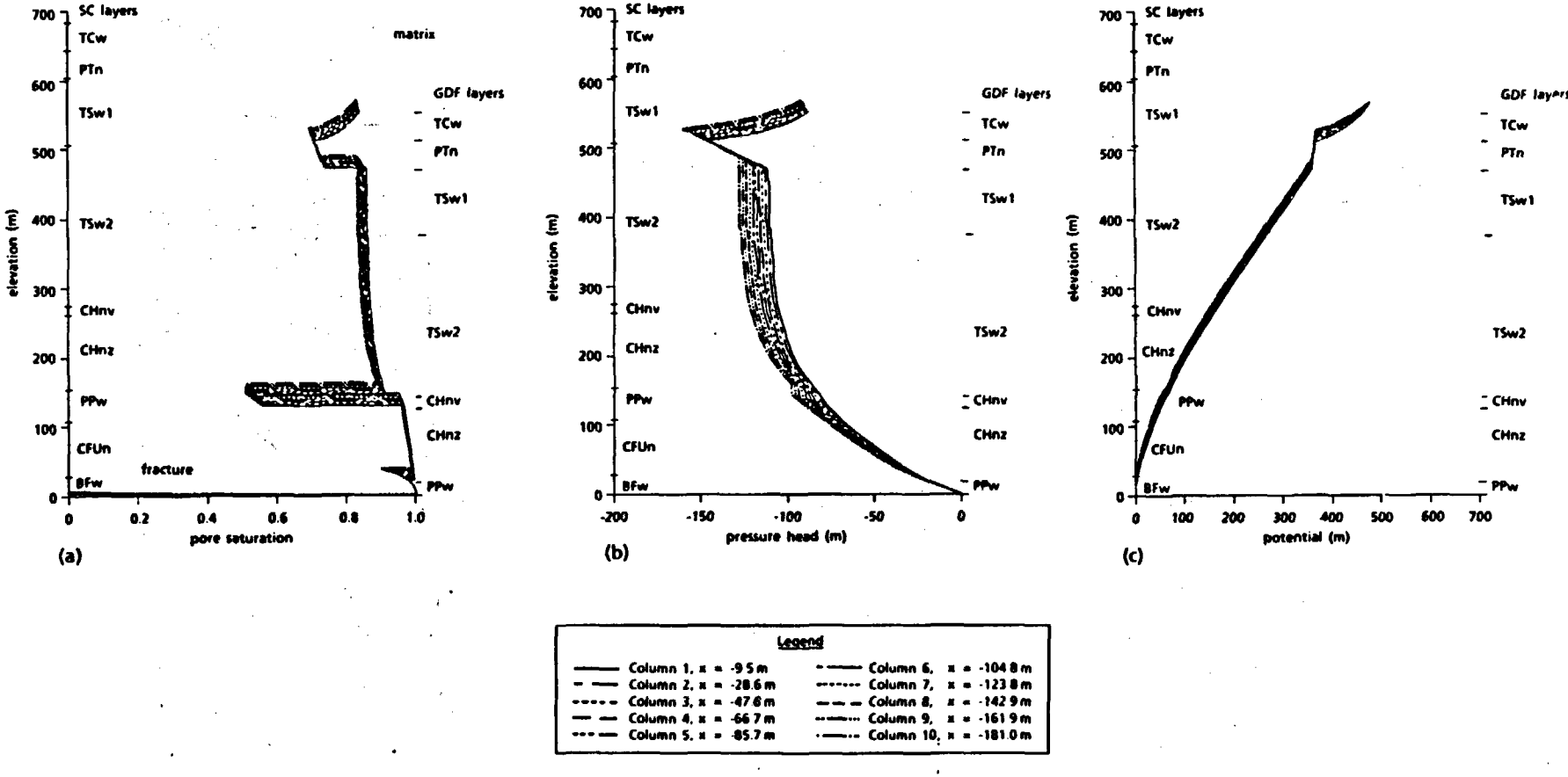

Figure 9. Plots of Elevation vs (a) Saturation, (b) Pressure Head, and (c) Potential for a 0.1-mm/yr Flux for a Ten-Even-Column (190-m) Section.

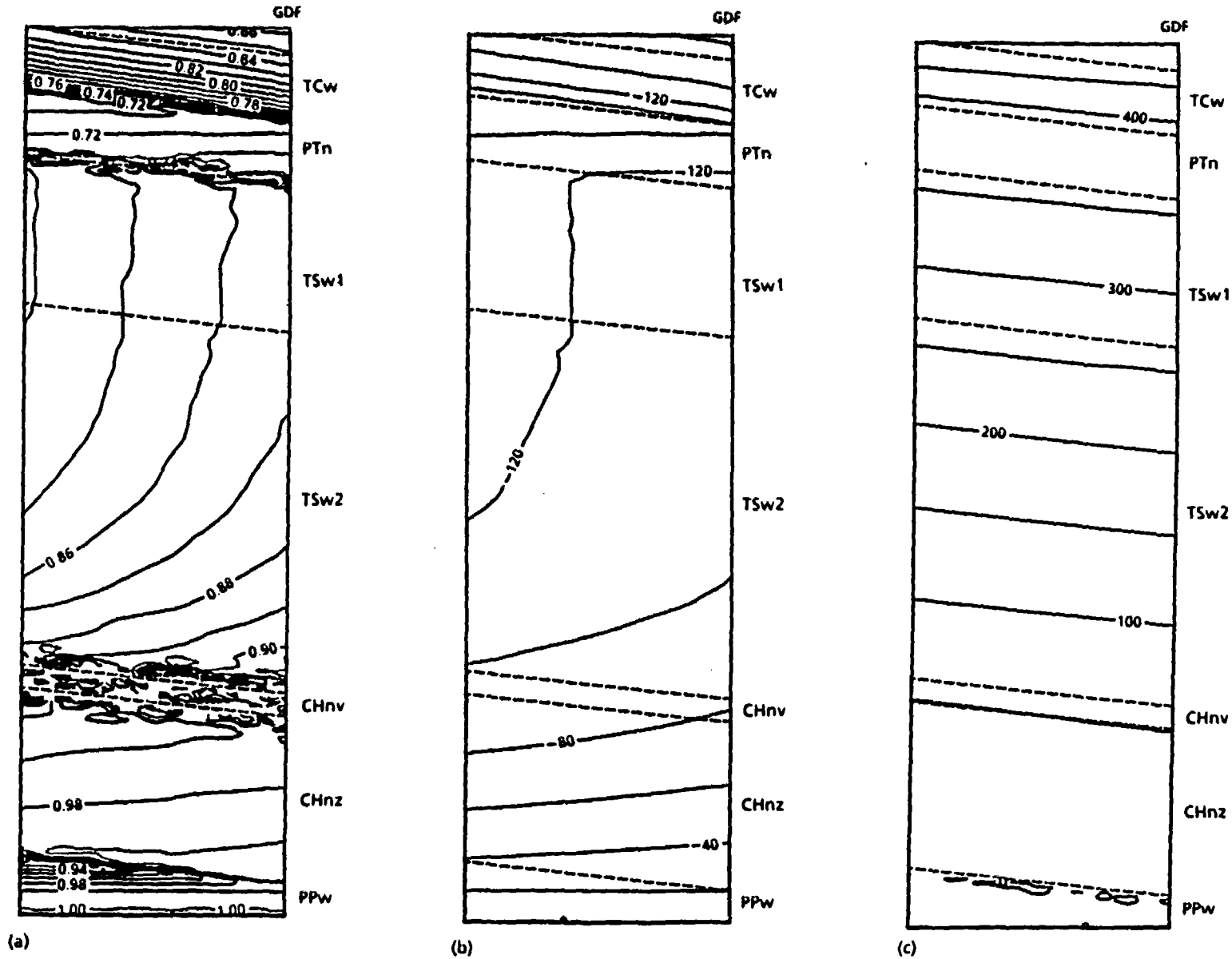

Figure 10. Contours of (a) Saturation, (b) Pressure Head, and (c) Potential for a 0.1-mm/yr Flux for a Ten-Even-Column (190-m) Section.

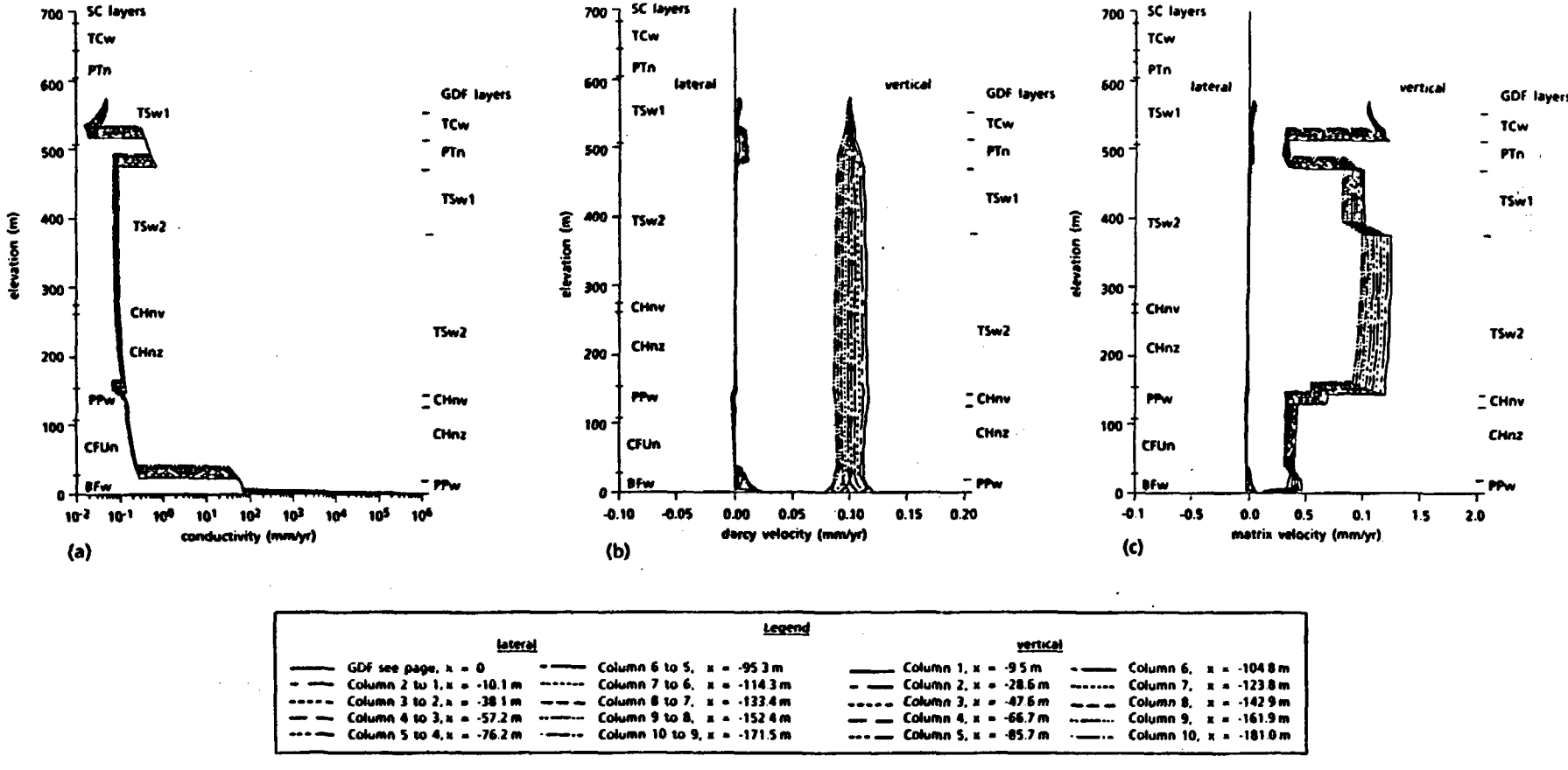

Figure 11. Plots of Elevation vs (a) Hydraulic Conductivity, (b) Darcy Velocity, and (c) Matrix Velocity for a 0.1-mm/yr Flux for a Ten-Even-Column (190-m) Section.

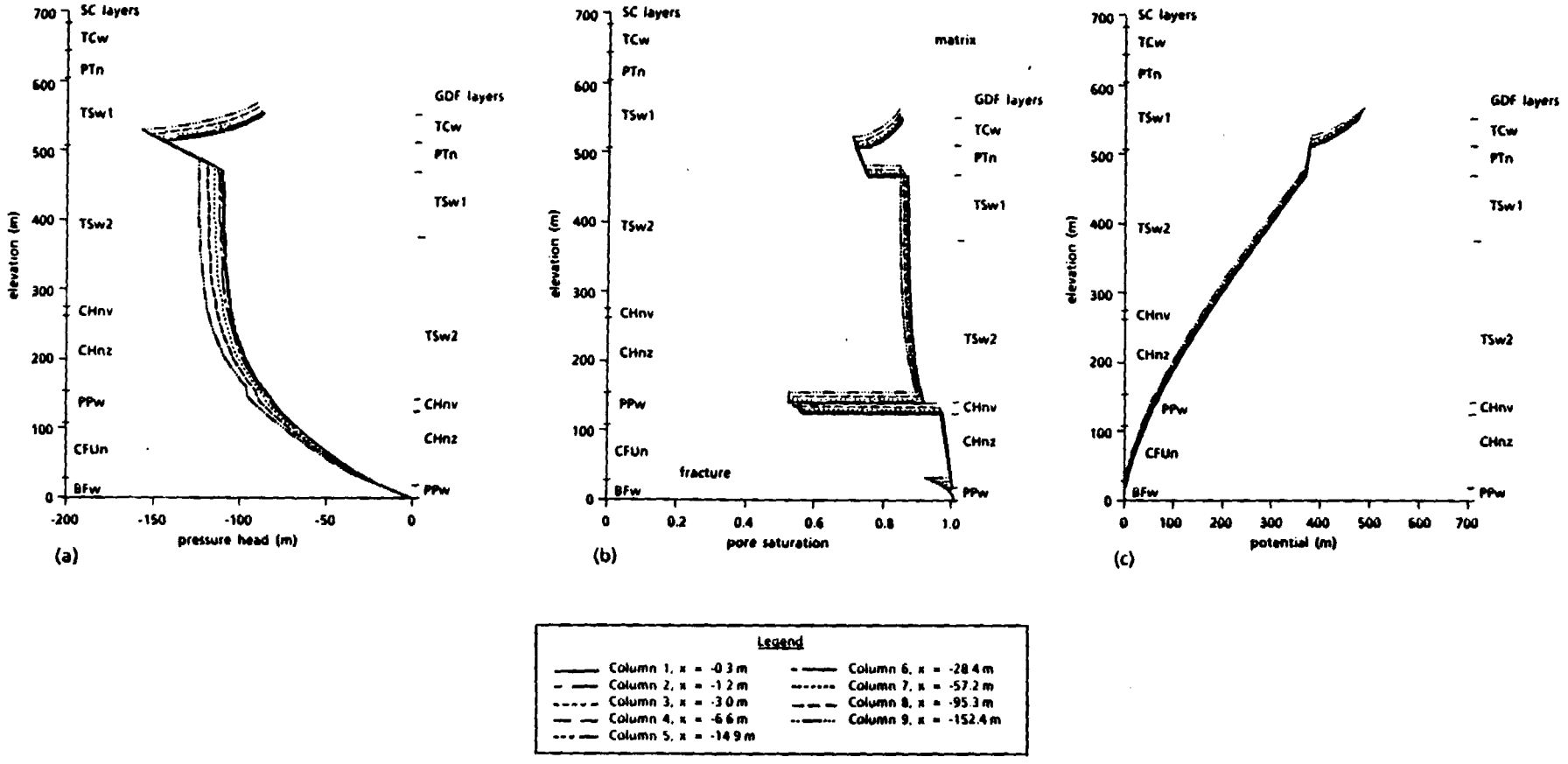

Figure 12. Plots of Elevation vs (a) Saturation, (b) Pressure Head, and (c) Potential for a 0.1-mm/yr Flux for a Nine-Nonuniform-Column (190-m) Section.

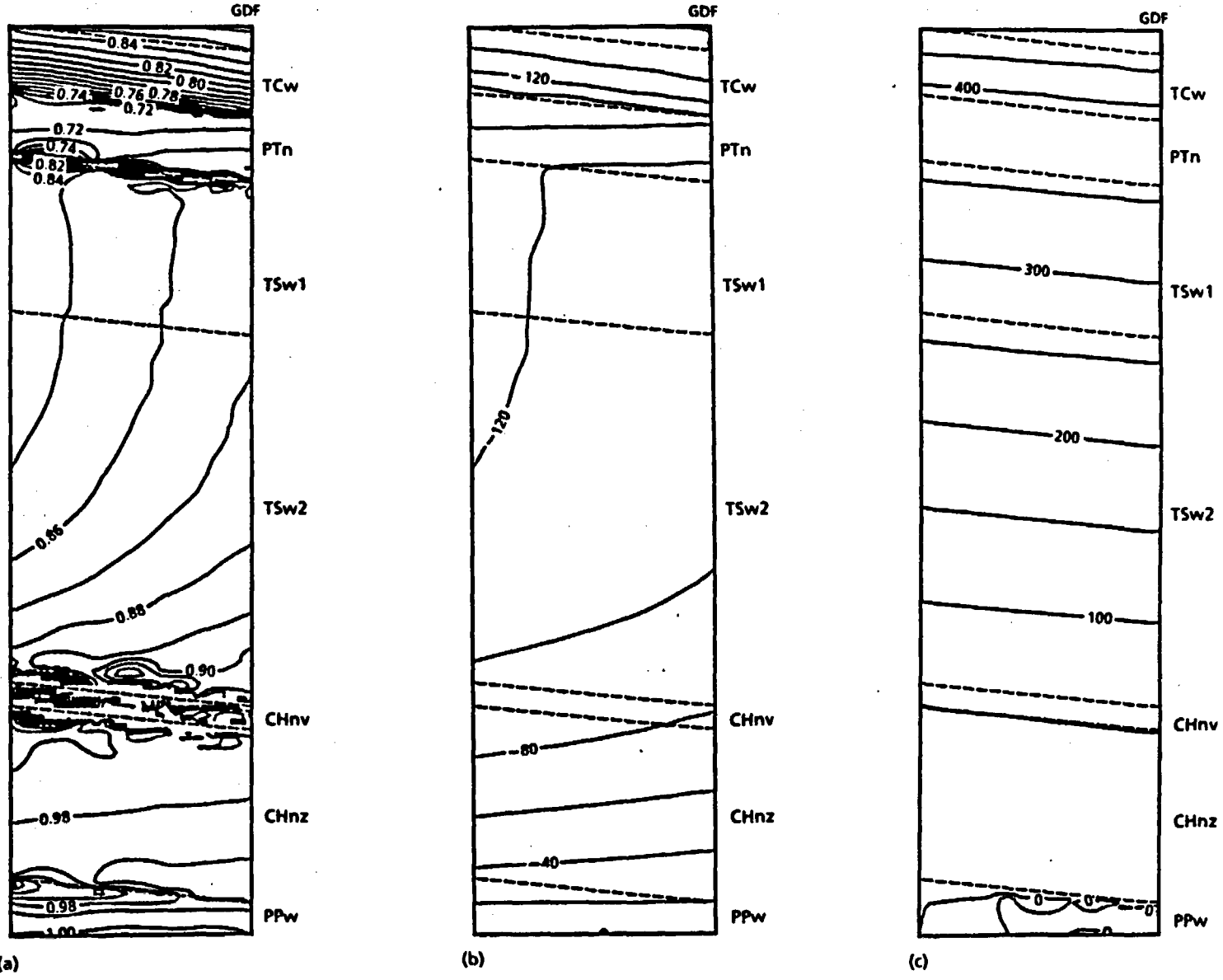

Figure 13. Contours of (a) Saturation, (b) Pressure Head, and (c) Potential for a 0.1-mm/yr Flux for a Nine-Nonuniform-Column (190-m) Section.

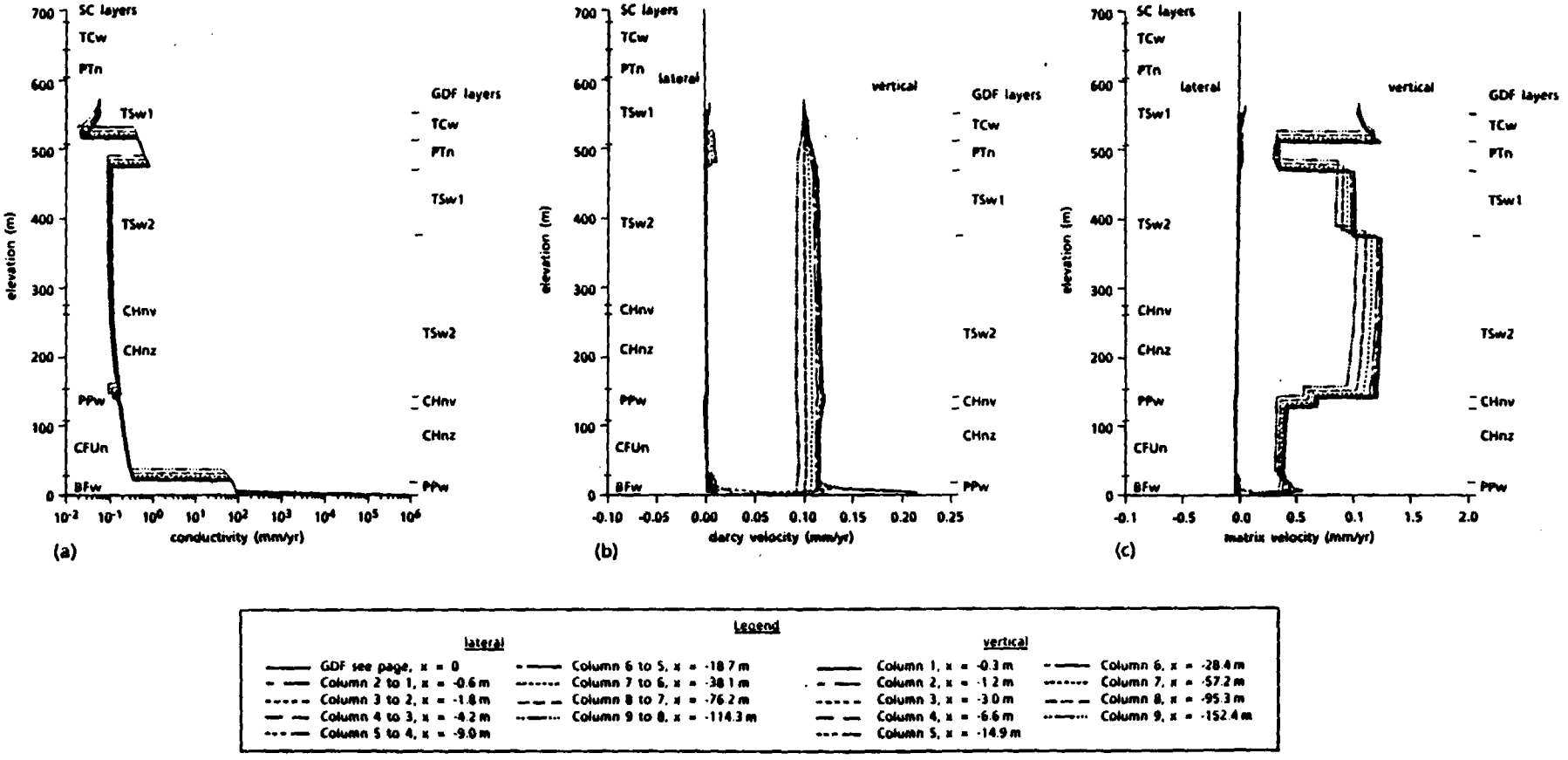

Figure 14. Plots of Elevation vs (a) Hydraulic Conductivity, (b) Darcy Velocity, and (c) Matrix Velocity for a 0.1-mm/yr Flux for a Nine-Nonuniform-Column (190-m) Section.

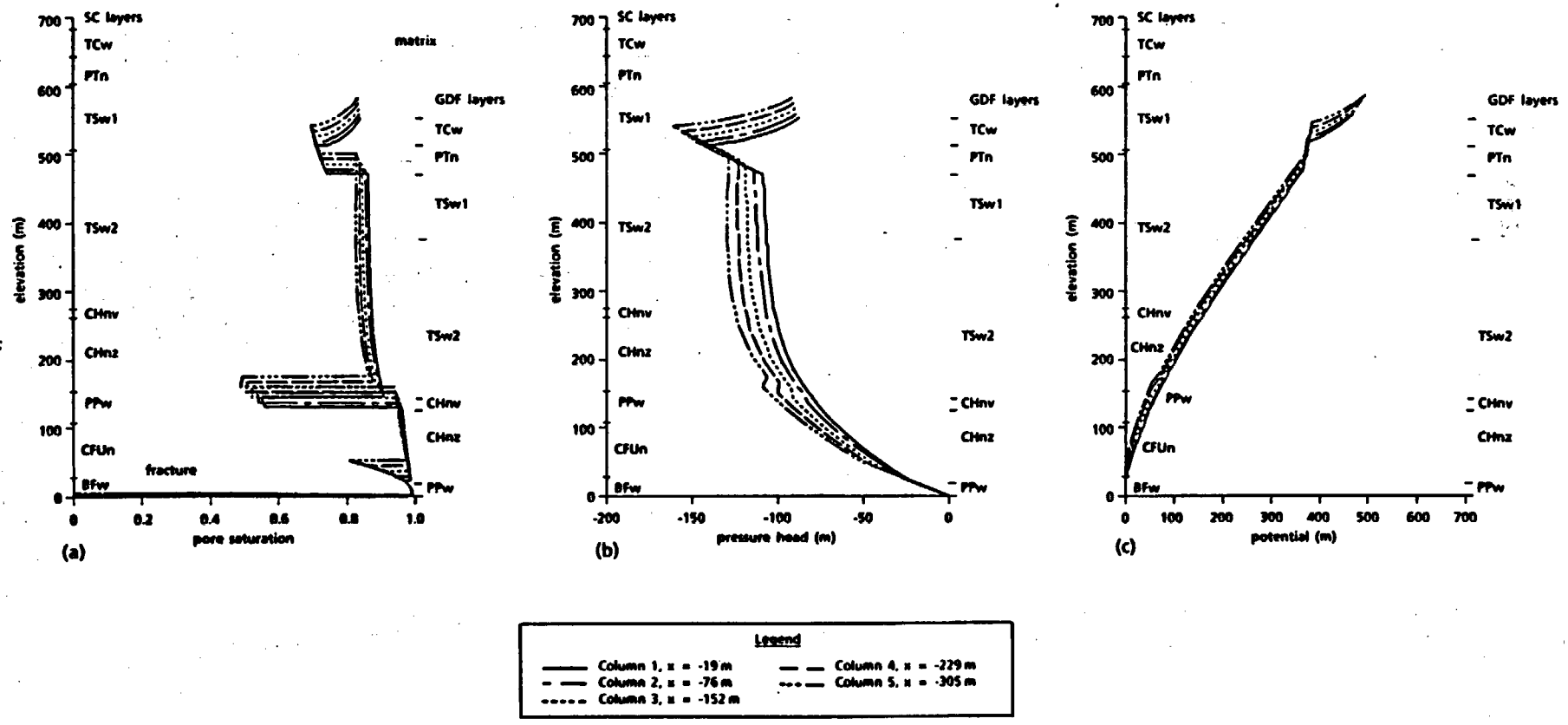

Figure 15. Plots of Elevation vs (a) Saturation, (b) Pressure Head, and (c) Potential for a 0.1-mm/yr Flux for a Five-Column (343-m) Section.

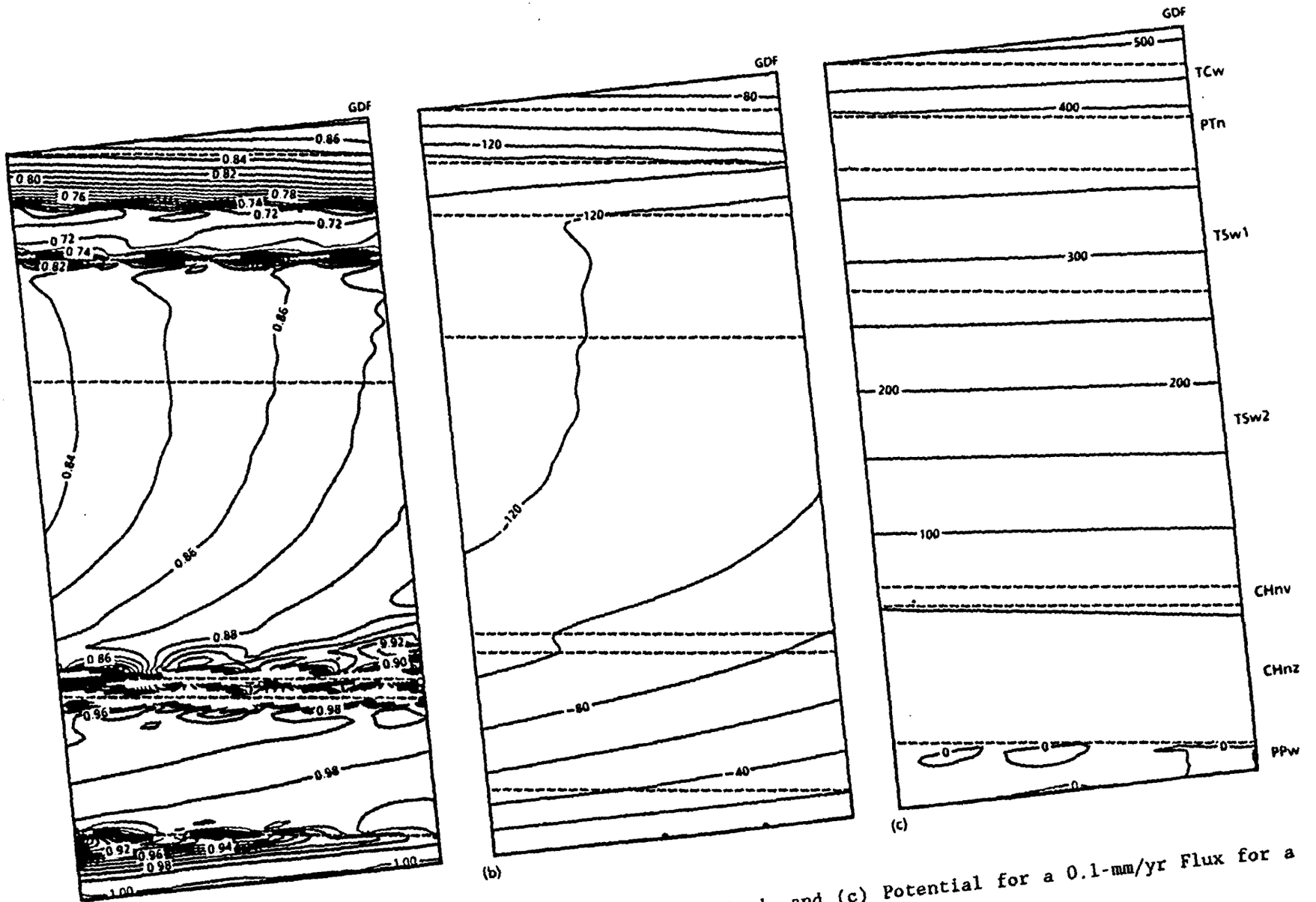

Figure 16. Contours of (a) Saturation, (b) Pressure Head, and (c) Potential for a 0.1-mm/yr Flux for a Five-Column (343-m) Section.

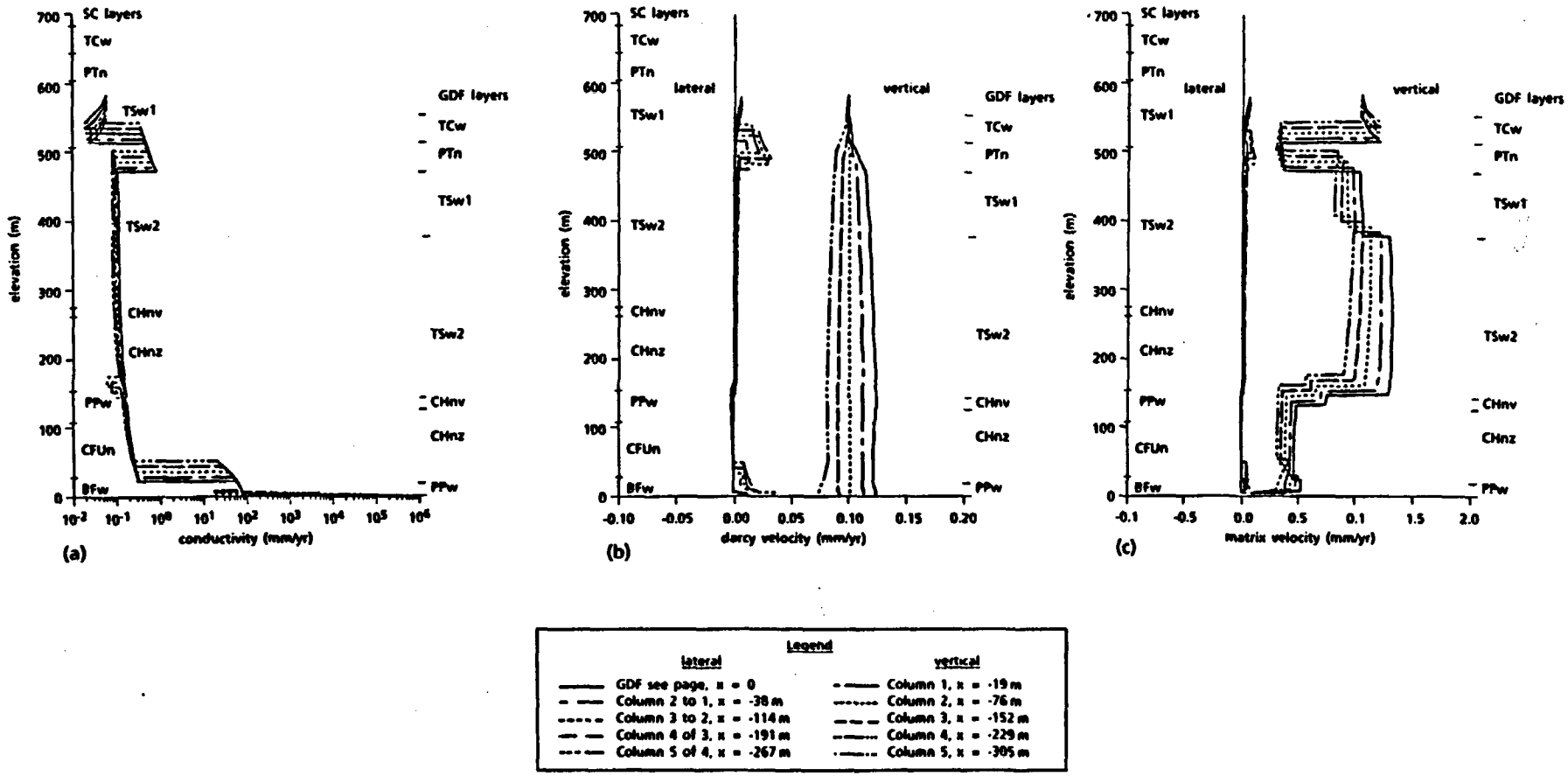

Figure 17. Plots of Elevation vs (a) Hydraulic Conductivity, (b) Darcy Velocity, and (c) Matrix Velocity for a 0.1-mm/yr Flux for a Five-Column (343-m) Section.

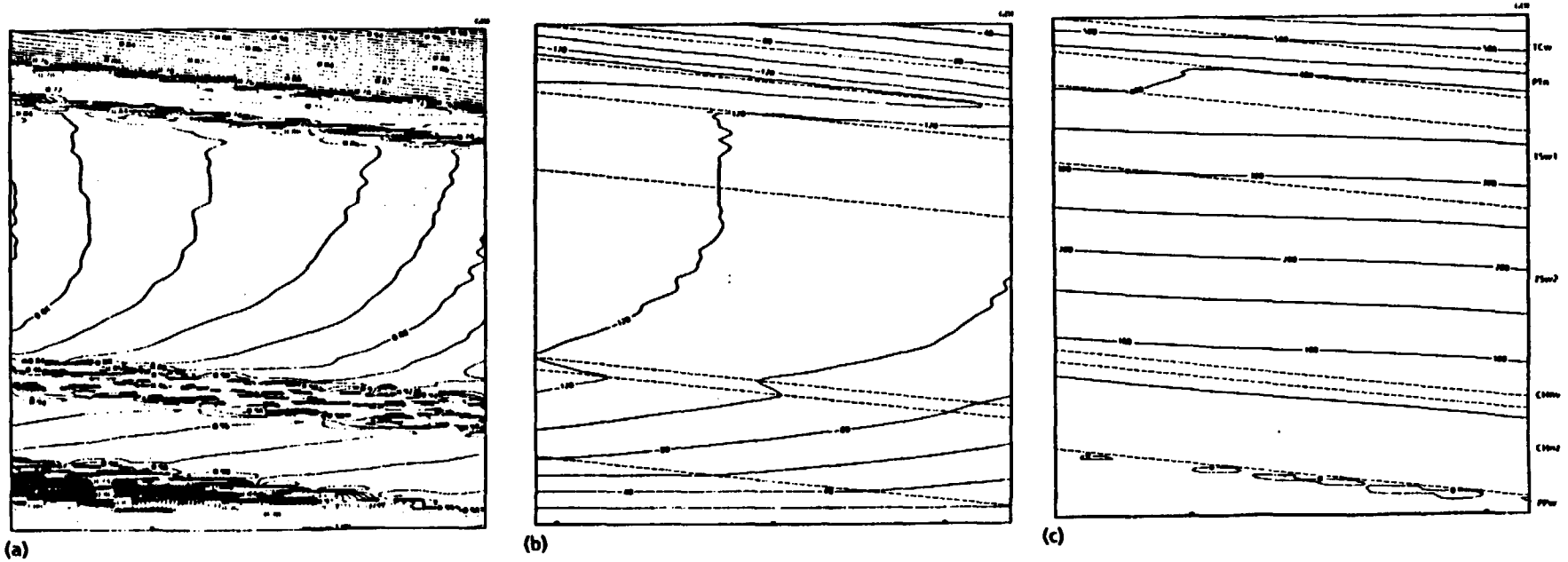

Figure 19. Contours of (a) Saturation, (b) Pressure Head, and (c) Potential for a 0.1-mm/yr Flux for a Nine-Column (645-m) Section.

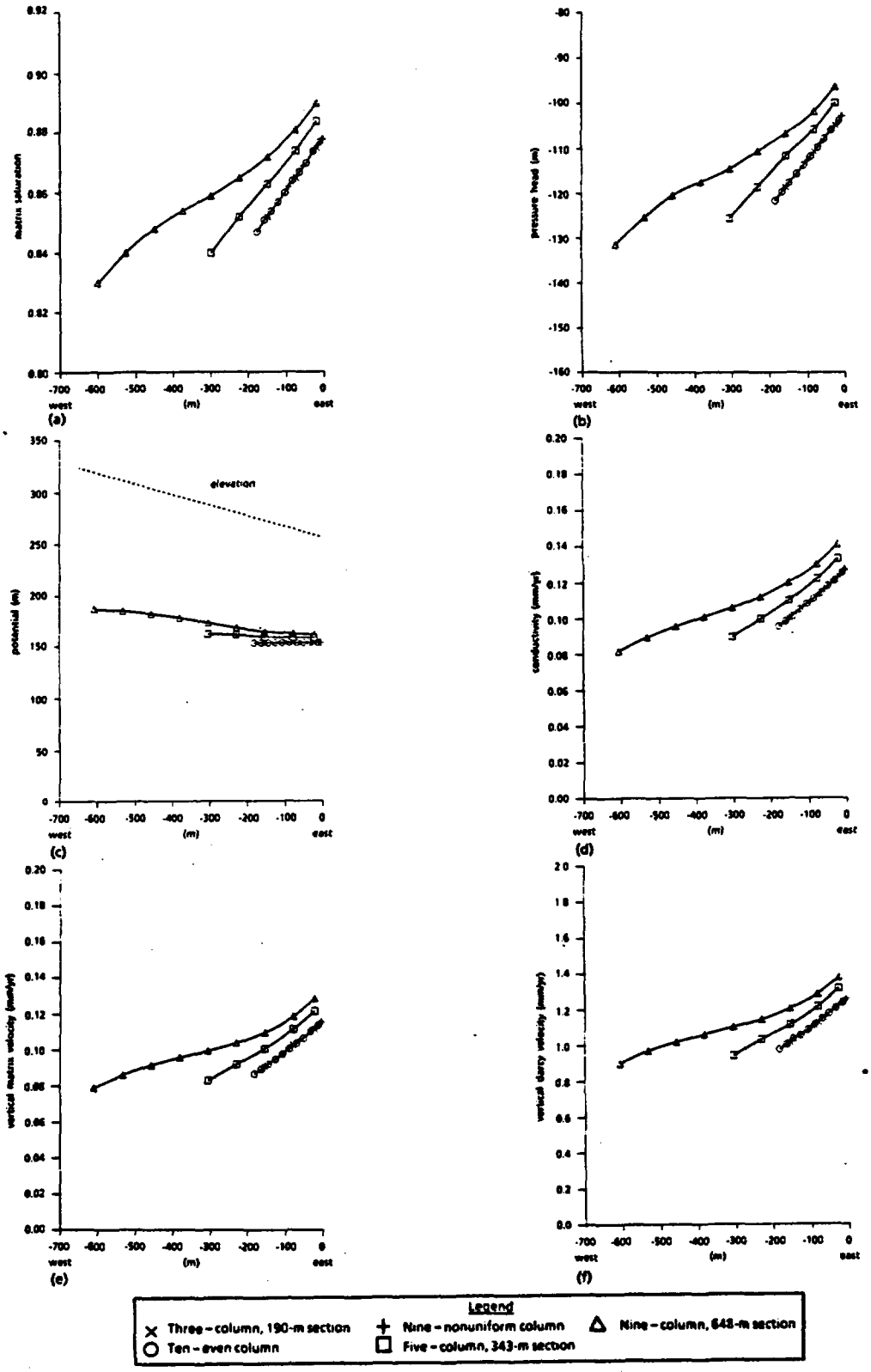

Figure 21. Lateral Distributions of (a) Matrix Saturation, (b) Pressure Head, (c) Potential, (d) Hydraulic Conductivity, (e) Vertical Matrix Velocity, and (f) Vertical Darcy Velocity in the Middle of the Topopah Spring Welded Unit (TSw2) with 0.1-mm/yr Flux.

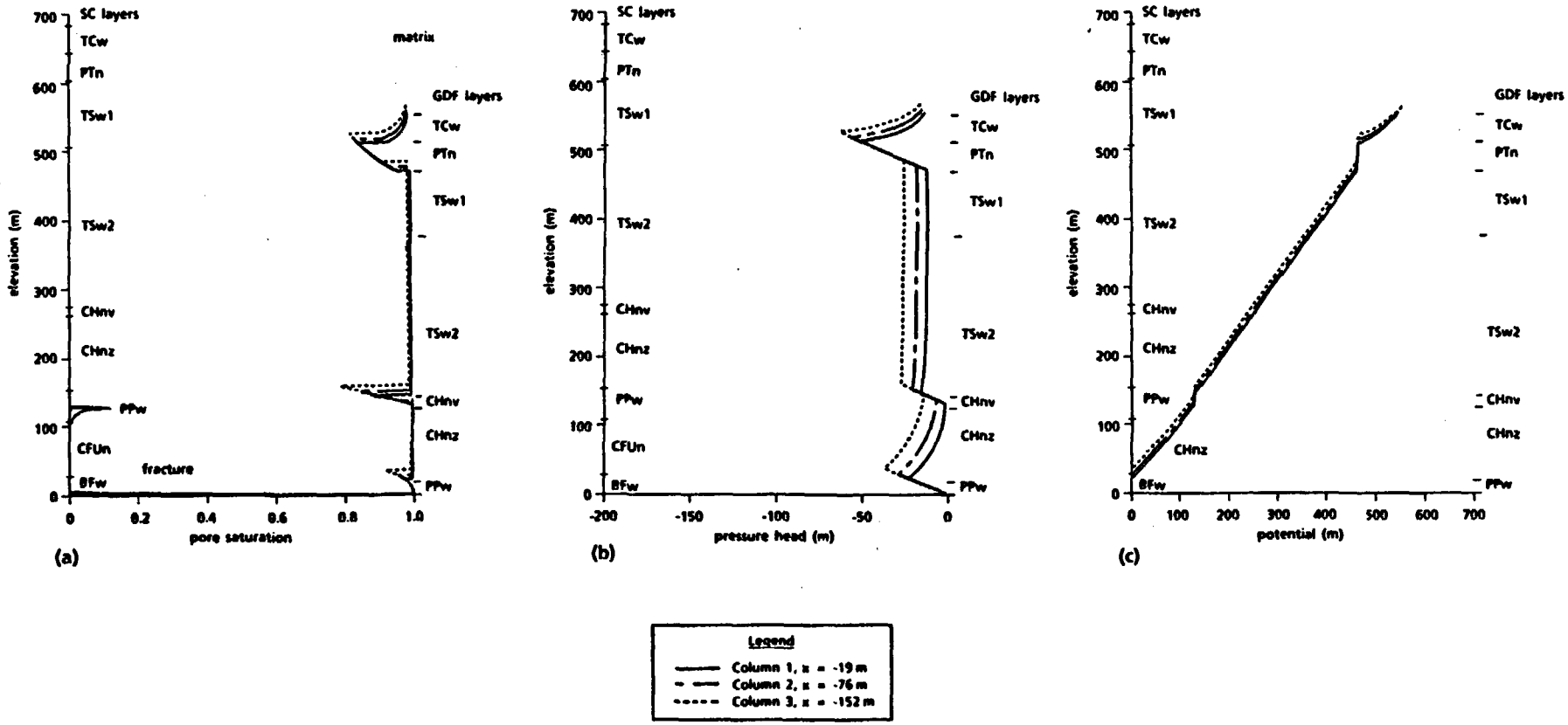

Figure 23. Plots of Elevation vs (a) Saturation, (b) Pressure Head, and (c) Potential for a 0.5-mm/yr Flux for a Three-Column (190-m) Section.

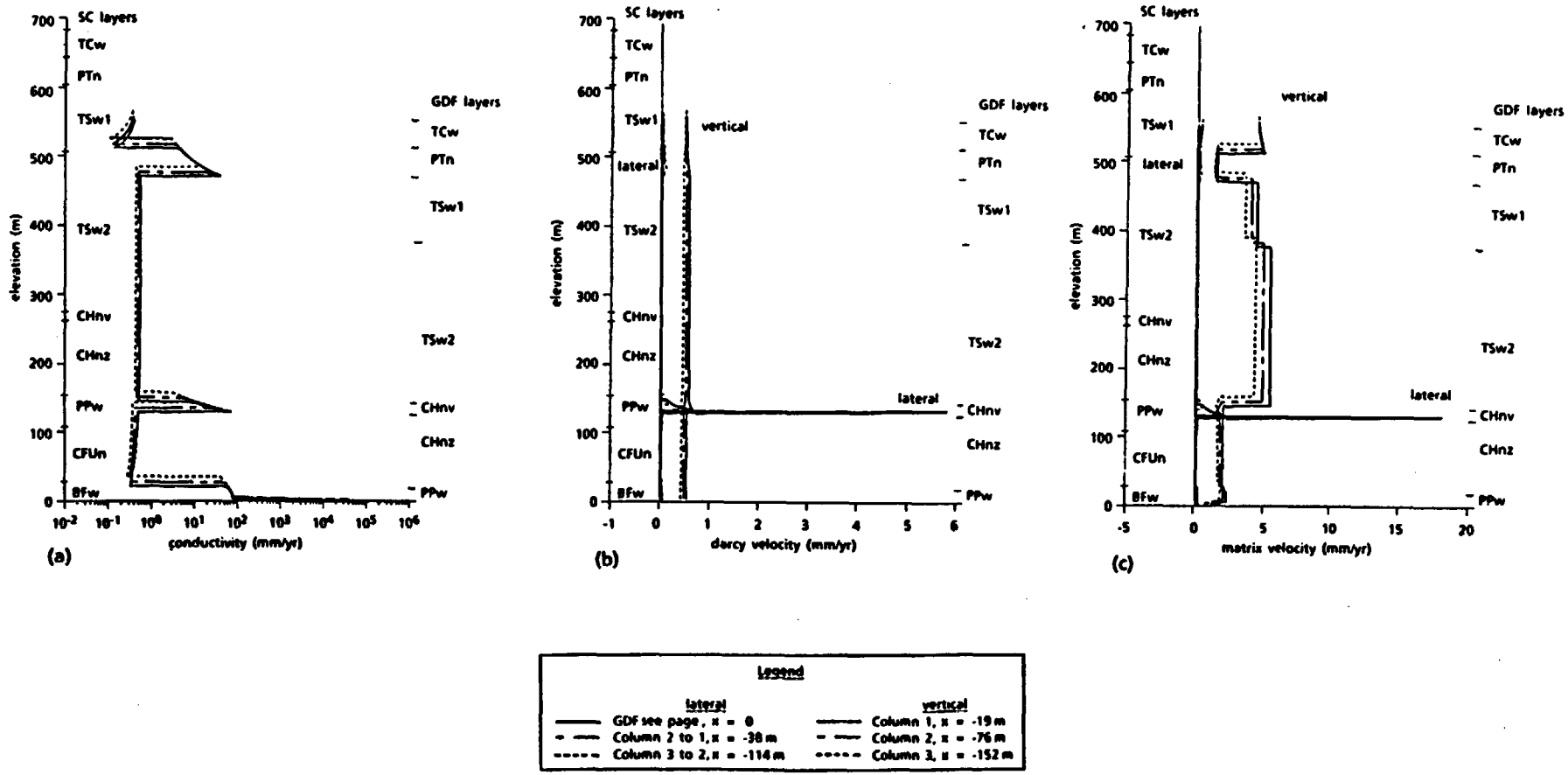

Figure 25. Plots of Elevation vs (a) Hydraulic Conductivity, (b) Darcy Velocity, and (c) Matrix Velocity for a 0.5-mm/yr Flux for a Three-Column (190-m) Section.

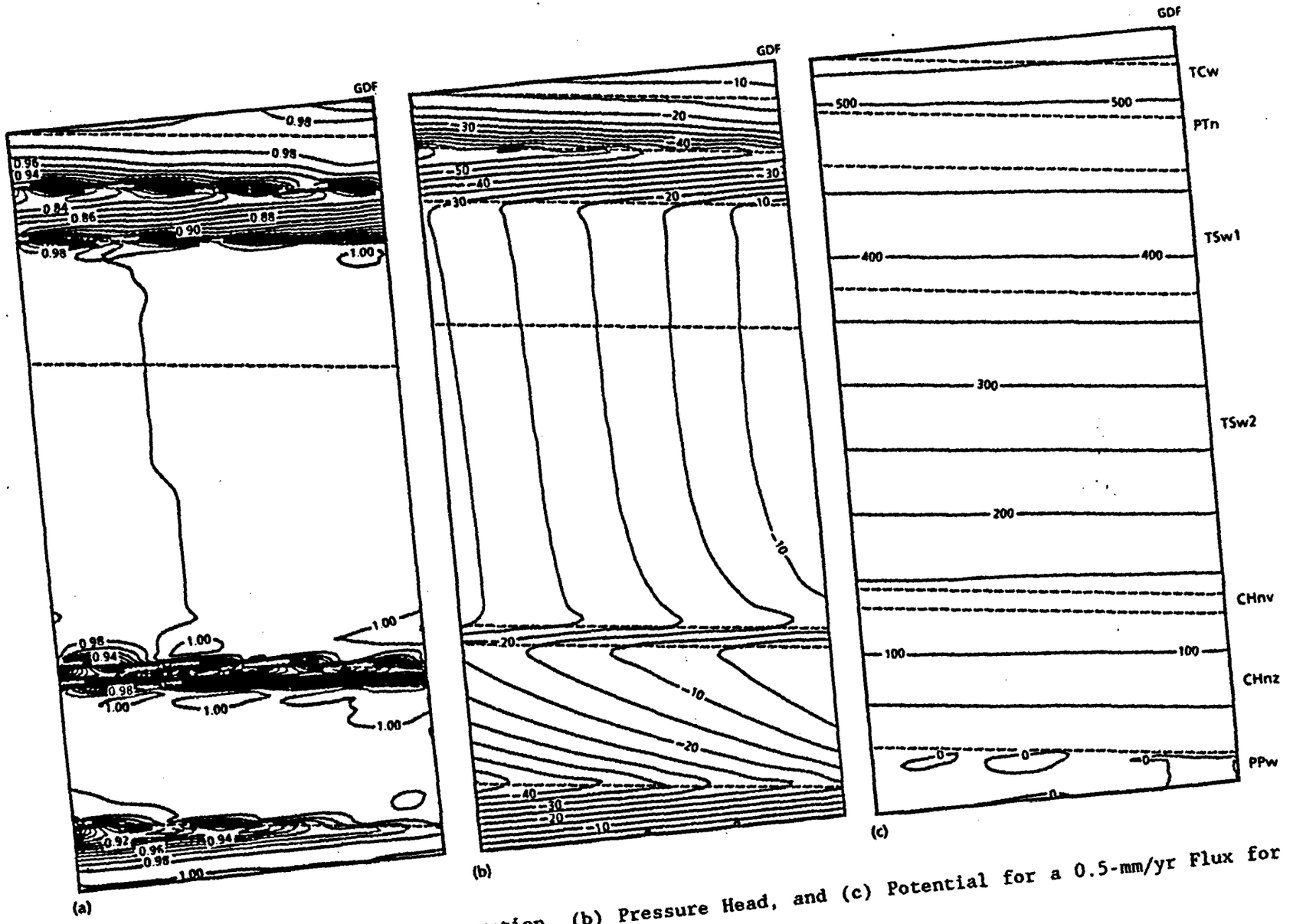

Figure 27. Contours of (a) Saturation, (b) Pressure Head, and (c) Potential for a 0.5-mm/yr Flux for a Five-Column (343-m) Section.

APPENDIX A

CORRELATION OF SATURATED AND PARTIALLY SATURATED FLOW PARAMETERS

In this appendix, we have compiled and compared the tuff hydrologic parameters tabulated and/or used in several previous reports. Specifically, we have focused on the laboratory matrix data and the sand fracture model in Peters et al. (1984) and Klavetter and Peters (1986); the matrix data and fracture/fault model in Rulon et al. (1986); and the fracture model parameters tabulated in this report (Table 3), which are deduced from fracture spacings in Wang and Narasimhan (1985). Although the available data base included in these reports may be limited and the models simple, we hope to gain some insight in understanding variabilities and trends in tuff hydrologic properties and to develop bounding guidelines for choosing model parameters. We have also examined whether there are statistically significant relationships and interdependencies among the flow parameters.

Saturated Conductivity Versus Characteristic Pore Size

Intuitively, we expect a coarse-grained, loosely packed medium to have large flow channels and high conductivity under saturated conditions, while a fine-grained, densely packed medium has small flow channels and low saturated conductivity. Under partially saturated conditions with negative suction pressures, large channels will be easily drained, while small channels may still hold water due to capillary forces. If this intuition is physical, we should expect a correlation between saturated conductivity and some of the parameters that characterize the desaturation process. One such parameter is air entry pressure.

The air entry pressure head can be easily defined by using the Brooks and Corey model (1966) for the saturation-pressure head relationship (characteristic curve):

$$\theta(h) = \left(\frac{h}{h_a}\right)^{-\lambda} = (-\alpha h)^{-\lambda} \text{ if } h \le h_a \qquad \text{(A1)}$$

and $\theta(h) = 1$ if $h > h_a$ • θ is the effective saturation

$$\theta = \frac{S - S_r}{S_s - S_r} \qquad \text{(A2)}$$

with the subscripts s and r indicating saturated and residual values of saturation S, respectively. In Equation A1, h_a is the air entry pressure head (also known as bubbling pressure in soil literature). The parameter $\alpha = -h_a^{-1}$ is used in other models. The parameter $\lambda \ge 0$ characterizes the slope of desaturation in the log (θ) versus log (-h) relationship. When the suction head h becomes more negative than the air entry head h_a, air enters the pores and water flows out of the medium to initiate desaturation. If flow channels are represented by capillary tubes or fractures, we can define air entry radius/aperture by the capillary equation

$$r_a = -\frac{2\sigma}{\rho g h_a} = \frac{2\sigma}{\rho g}\alpha \quad . \qquad \text{(A3)}$$

Figure A-1a is the saturated-conductivity versus air entry radius/aperture plot from the three different data sets and models. Each set is plotted separately in Figures A-1b, c, and d with the tuff units labeled. The tuff matrix data in Figure A-1b are based on laboratory measurements of 1.4- x 1.2-cm (diameter x length) cylinders subcored from core samples of Boreholes USW G-4 and USW GU-3 (Table A.2 of Peters et al., 1984). For some core samples, saturated conductivity values from different subcores varied, and two points were plotted in Figure A-1b to correspond to the range of measured values. For a few samples, only the upper bound of saturated conductivity was measured and plotted. The saturated conductivity values for fractures in Figure A-1b were determined from saturated flow measurements of fractured cores under stress. Characteristic parameters of a typical sand were chosen to describe the desaturation behavior of fractures (Klavetter and Peters, 1986).

Figure A-1c is based on the data and parameters used by Rulon et al. (1986) in a large-scale (10^3 - 10^4 m) simulation study of potential lateral diversions of infiltration into fault zones. For fault zones on the side boundaries and for the Tiva Canyon welded unit (TCw) on the top, fracture flow conditions were assumed and fracture saturation-pressure relationships were given in the Brooks-Corey form, with parameters determined by a theoretical model of Harrold et al. (1985). Van Genuchten parameters were given for the Paintbrush nonwelded unit (PTn), the matrix of the Topopah Spring unit (TSw), and the Calico Hills nonwelded, vitric unit (CHnv). In addition to the matrix flow condition, the TSw unit was also modeled as a fracture-flow-only unit and as a fracture-matrix composite medium. Horizontal saturated conductivities were assumed to be ten times the vertical values for the nonwelded PTn and CHnv units. Vertical saturated conductivity was assumed to be fifty times the horizontal value for the fault zone. For the fault and for fractures, the saturated conductivities plotted in Figure A-1c correspond to the bulk conductivity values divided by porosities. Because porosities in the original tables of Rulon et al. (1986) may correspond to total instead of fracture porosities, saturated conductivities in Figure A-1c for the fault and for the fractures are probably low. Rulon et al. (1986) also studied the effects of changing air entry pressure of fracture characteristic curves of welded units by two orders of magnitude.

Figure A-1d was plotted with fracture parameters given in Table 3 in the text. In terms of parameters β and b_c, the saturated permeability of a discrete fracture is (Wang and Narasimhan, 1985)

$$k_s = \frac{b^2}{12} = \frac{1}{12}\left[\frac{6(4+\beta b_c)}{\beta^3}\exp(-\beta b_c)\right]^{2/3} \quad . \qquad (A11)$$

If we neglect, for the moment, the dependencies of both the saturated permeability in Equation A11 and the air entry aperture in Equation A10 on the combined parameters βb_c, k_s is proportional to β^{-2}, r_a is proportional to β^{-1}, and, therefore, the approximate dependence of k_s is proportional to r_a^2. In the log-log plot shown in Figure A-1d, the square dependence is manifested as a straight line with Slope 2. The saturated permeability k_s and the air entry aperture r_a also depend on the combined parameter βb_c. For fractures of the TCw unit on top with a low overburden stress, fracture contact areas and corresponding contact apertures b_c are smaller than

Brooks-Cory and the van Genuchten models is the exponent λ or n. The exponent in the saturation-pressure head relationship also determines the relative conductivity function if we use some theoretical models. One such theory was given by Mualem (1976) to predict relative conductivity from a saturation-pressure curve. Maulem (1976) assumed that flow channels in a porous medium were composed of capillary tubes with varying radii. If two tubes were connected in series, the ratio of the tube lengths was assumed to be proportional to the ratio of the tube radii. With this correlation between tube length and tube radius, Mualem (1976) derived the relative conductivity function

$$k_r(\theta) = \theta^{1/2} \left[\frac{\int_0^{\theta} \frac{1}{h(s)}\, ds}{\int_0^{1} \frac{1}{h(s)}\, ds} \right]^2 . \qquad \text{(A12)}$$

If Equation A1 is used in Equation A12,

$$k_r(\theta) = \theta^{2.5+2/\lambda} \qquad \text{(A13)}$$

and

$$k_r(h) = (-\alpha h)^{-(2+2.5\lambda)} \qquad \text{(A14)}$$

as shown by van Genuchten (1980). Van Genuchten also used Equation A4 to derive

$$k_r(\theta) = \theta^{1/2} [1 - (1 - \theta^{1/m})^m]^2 \qquad (m = 1 - 1/n) \qquad \text{(A15)}$$

and

$$k_r(h) = \frac{1 - (-\alpha h)^{n-1}[1 + (-\alpha h)^n]^{-m^2}}{[1 + (-\alpha h)^n]^{m/2}} \qquad (m = 1 - 1/n) \; . \qquad \text{(A16)}$$

For large negative values of pressure head, Equation A16 is asympotically equal to Equation A14 with $\lambda = n - 1$. Therefore, the log (k_r) versus log (-h) relationship is characterized by $2 + 2.5\lambda$. Figures A-3a, b, and c are plots of saturated conductivity versus this relative conductivity slope.

If we examine only the tuff matrix data in Figure A-3b and ignore the sand fracture points, there is a weak correlation between the saturated conductivity and the slope of relative conductivity. If this correlation is established statistically, a permeable medium under a saturated condition will be easily drained by a negative suction pressure. In Figure A-3c, the few points do not show such a correlation. In Rulon et al. (1986), the exponents of the relative conductivity curves for the fault and fractures were given independently and not derived from the exponent of saturation-pressure curves. The values of the exponent λ for the saturation-pressure curves were approximately $2(\lambda = 1/0.497$ for fault and $\lambda = 1/0.491$ for fractures). Values of the exponent for log (k_r) versus log (-h) curves were approximately 4(1.945/0.497 for fault and 1.936/0.491 for fractures). If the Mualem theory is used, a $\lambda = 2$ characteristic

Without taking the phase constriction effect into account (by setting $\tau = 1$) and using only the average cubic aperture factor, the exponent of pressure dependence is 4. The cubic aperture factor alone assumes that all flow channels in the fracture plane are parallel. When flow channels are parallel, conductivities from different channels are additive in determining the total conductivity of the system. When large channels are drained, liquid will flow along small channels separated by large dry channels. If a fracture surface is characterized by parallel channels, conductivity will be highly anisotropic. Normal to channel direction, there will be no flow when the largest channel is drained and effective conductivity drops to zero. Certainly most rock fracture surfaces have no such idealistic parallel channel pattern. The log (k_r) versus log (-h) slopes of ≈ 4 in Figure A-3c for the fault and fractures may be too small. If relative conductivity of a medium drops slowly while saturation drops quickly as pressure descreases, the medium can become very dry but still maintain high conductivity, as shown in Figures A-5a and b.

It is also of interest to note that the Mualem or Burdine theory for porous media takes into account the effect of capillary tubes in series. The cubic aperture average factor alone does not consider any possibility that flow channels can be connected in series. The phase constriction factor was introduced in Wang and Narasimhan (1985) to correct for unrealistic characteristics of parallel flow channels in simple cubic law. Conductivities are sensitive to channel-in-series effects. Cubic law may overestimate conductivity under partially saturated conditions with high negative pressure values.

Summary

In studying heterogeneous systems with faults and fractures together with porous flow regions, if the conductivities of faults or fractures are overestimated relative to the porous medium, corresponding fault and fracture flows may also be overestimated. In the absence of data on relative conductivity under partially saturated conditions, theoretical models were used for the fault/fracture and porous tuff units. If the model for the porous medium takes into account the channel-in-series effect, the use of a generalized cubic aperture law without considering the channel-in-series effect may overestimate the fault/fracture conductivities under partially saturated conditions. In this appendix, we have analyzed available data and have compared models to assess characteristic parameters of saturation and relative conductivity. Saturated conductivity appears to be correlated with sizes of the largest channels and the average capillary channels. Saturated conductivity may also be correlated with the slope of relative conductivity, which measures how easily the medium loses its conductivity under negative pressure. A loose medium with high saturated conductivity usually is more easily drained than a tight medium with low saturated conductivity. If correlations between saturated conductivity and partially saturated characteristic parameters can be shown to be statistically significant, it will be valuable to substantiate the role reversal between fractures and porous medium and between fault and formation in the transition from saturated conditions to partially saturated conditions.

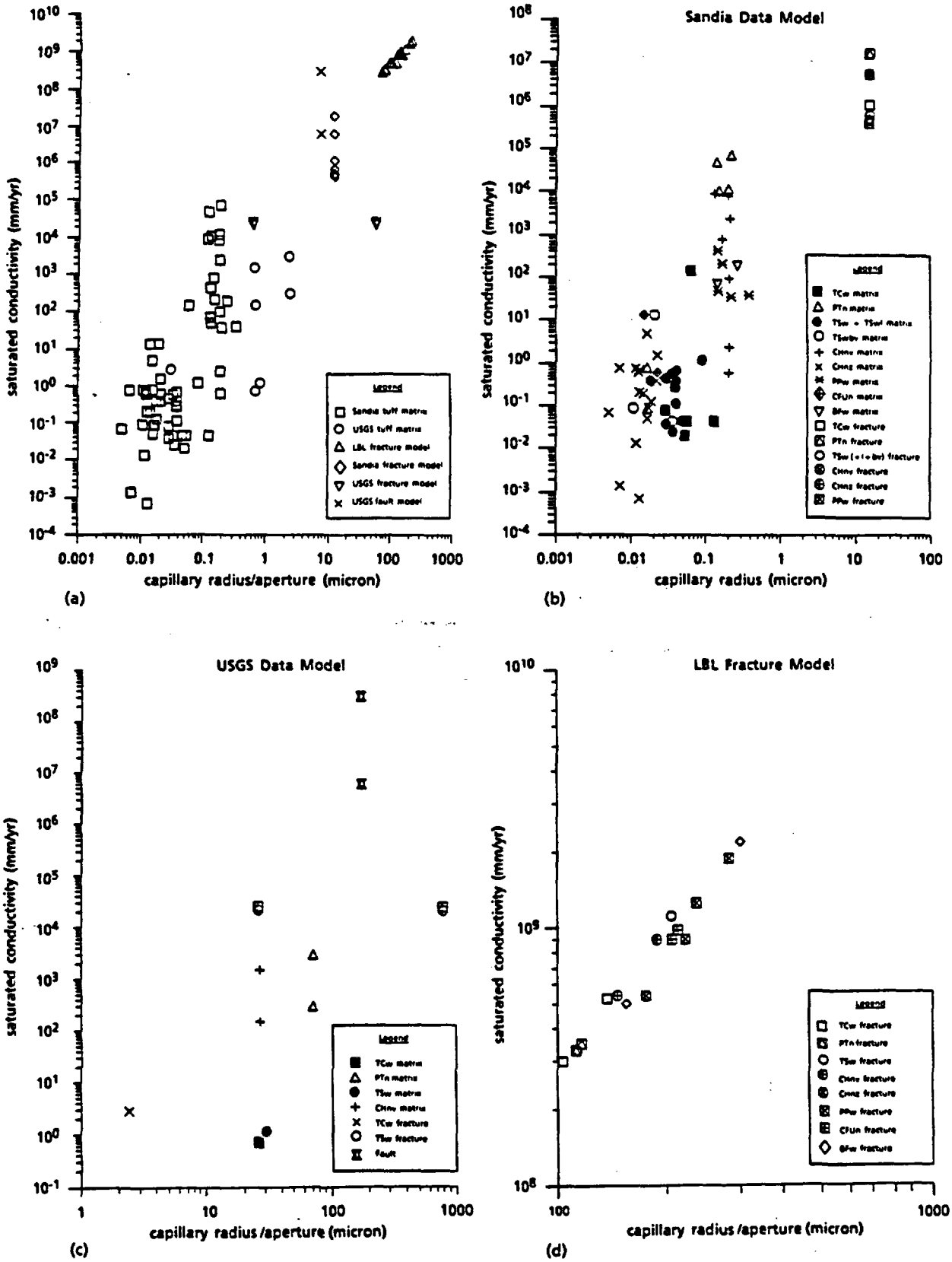

Figure A-2. Correlation Between Saturated Conductivity and Capillary Radius/Aperture.

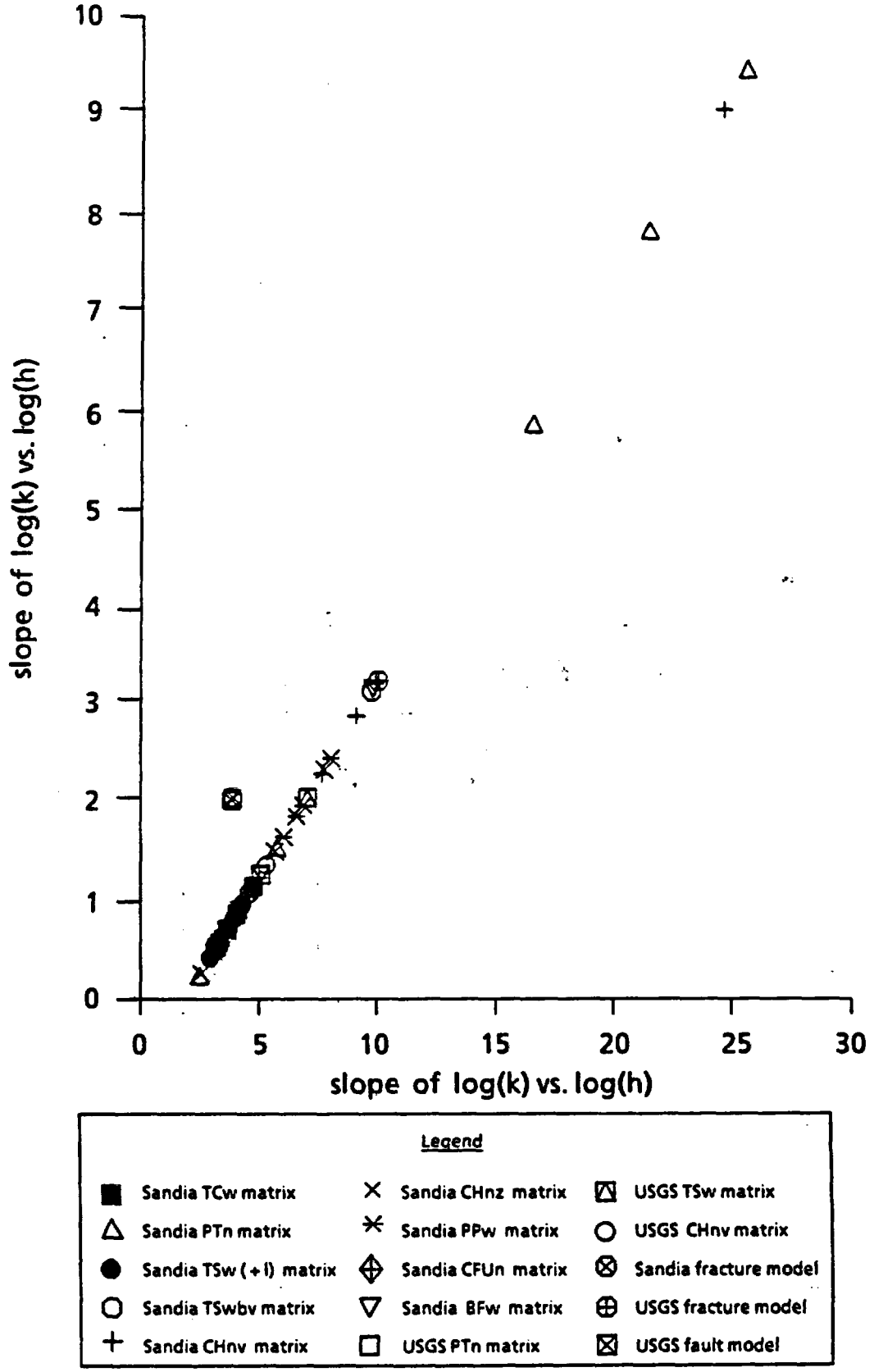

Figure A-4. Relationship Between the Exponents of Saturation Characteristic Curve and Relative Permeability Characteristics Curve.

APPENDIX B

INFORMATION RELEVANT TO THE REFERENCE INFORMATION BASE

B-1. The following are sources of data used in this report.

1. Tables 1, 2, and 3 contain information for hydrologic data used in the report. All data were taken from NNWSI Reference Information Base (RIB, April 1986) and from Sinnock et al. (1984); Peters et al. (1984); Ortiz et al. (1984); Nimick et al. (1984); Thordarson (1983); Spengler and Chornack (1984); and Wang and Narasimhan (1985).

2. Figure 4 shows the grids of two-dimensional cross section models.

B-2. Data Recommended for Inclusion in the Reference Information Base:

No results are candidate for inclusion in the RIB.

B-3. Data Recommended for Inclusion in the Tuff Data Base:

None.

DISTRIBUTION LIST

C. E. Kay, Acting Director (RW-1)
Office of Civilian Radioactive
Waste Management
U.S. Department of Energy
Forrestal Bldg.
Washington, D.C. 20585

Ralph Stein (RW-30)
Office of Civilian Radioactive
Waste Management
U.S. Department of Energy
Forrestal Bldg.
Washington, D.C. 20585

M. W. Frei (RW-22)
Office of Civilian Radioactive
Waste Management
U.S. Department of Energy
Forrestal Bldg.
Washington, D.C. 20585

B. G. Gale (RW-23)
Office of Civilian Radioactive
Waste Management
U.S. Department of Energy
Forrestal Bldg.
Washington, D.C. 20585

Samuel Rousso (RW-10)
Office of Civilian Radioactive
Waste Management
U.S. Department of Energy
Forrestal Bldg.
Washington, D.C. 20585

J. D. Saltzman (RW-20)
Office of Civilian Radioactive
Waste Management
U.S. Department of Energy
Forrestal Bldg.
Washington, D.C. 20585

S. J. Brocoum (RW-221)
Office of Civilian Radioactive
Waste Management
U.S. Department of Energy
Forrestal Building
Washington, D.C. 20585

V. J. Cassella (RW-123)
Office of Civilian Radioactive
Waste Management
U.S. Department of Energy
Forrestal Bldg.
Washington, D.C. 20585

S. H. Kale (RW-20)
Office of Civilian Radioactive
Waste Management
U.S. Department of Energy
Forrestal Bldg.
Washington, D.C. 20585

T. H. Isaacs (RW-40)
Office of Civilian Radioactive
Waste Management
U.S. Department of Energy
Forrestal Bldg.
Washington, D.C. 20585

D. H. Alexander (RW-332)
Office of Civilian Radioactive
Waste Management
U.S. Department of Energy
Forrestal Bldg.
Washington, D.C. 20585

C. Bresee (RW-10)
Office of Civilian Radioactive
Waste Management
U.S. Department of Energy
Forrestal Bldg.
Washington, D.C. 20585

Gerald Parker (RW-333)
Office of Civilian Radioactive
Waste Management
U.S. Department of Energy
Forrestal Bldg.
Washington, D.C. 20585

Chief, Repository Projects Branch
Division of Waste Management
U.S. Nuclear Regulatory Commission
Washington, D.C. 20555

James C. Calovini
Technical Project Officer for NNWSI
Holmes & Narver, Inc.
101 Convention Center Dr.
Suite 860
Las Vegas, NV 89109

Dr. David W. Harris
NNWSI Technical Project Officer
Bureau of Reclamation
P.O. Box 25007 Bldg. 67
Denver Federal Center
Denver, CO 80225-0007

M. D. Voegele
Science Applications International Corp.
101 Convention Center Dr.
Suite 407
Las Vegas, NV 89109

J. A. Cross, Manager
Las Vegas Branch
Fenix & Scisson, Inc.
P.O. Box 93265
Mail Stop 514
Las Vegas, NV 89193-3265

P. T. Prestholt
NRC Site Representative
1050 East Flamingo Road
Suite 319
Las Vegas, NV 89119

A. E. Gurrola, General Manager
Energy Support Division
Holmes & Narver, Inc.
P.O. Box 93838
Mail Stop 580
Las Vegas, NV 89193-3838

B. L. Fraser, General Manager
Reynolds Electrical & Engineering Co.
P.O. Box 98521
Mail Stop 555
Las Vegas, NV 89193-8521

P. K. Fitzsimmons, Director
Health Physics & Environmental Division
Nevada Operations Office
U.S. Department of Energy
P.O. Box 98518
Las Vegas, NV 89193-8518

Robert F. Pritchett
Technical Project Officer for NNWSI
Reynolds Electrical & Engineering Co.
P.O. Box 98521
Mail Stop 615
Las Vegas, NV 89193-8521

Elaine Ezra
NNWSI GIS Project Manager
EG&G Energy Measurements, Inc.
P.O. Box 1912
Mail Stop H-02
Las Vegas, NV 89125

SAIC-T&MSS Library (2)
Science Applications International Corp.
101 Convention Center Dr.
Suite 407
Las Vegas, NV 89109

Dr. Martin Mifflin
Desert Research Institute
Water Resources Center
2505 Chandler Avenue
Suite 1
Las Vegas, NV 89120

E. P. Binnall
Field Systems Group Leader
Building 50B/4235
Lawrence Berkeley Laboratory
Berkeley, CA 94720

T. G. Barbour
Science Applications International Corp.
1626 Cole Blvd., Suite 270
Golden, CO 80401

Department of Comprehensive Planning
Clark County
225 Bridger Avenue, 7th Floor
Las Vegas, NV 89155

Economic Development Department
City of Las Vegas
400 East Stewart Avenue
Las Vegas, NV 89109

Planning Department
Nye County
P.O. Box 153
Tonopah, NV 89049

Director of Community Planning
City of Boulder City
P.O. Box 367
Boulder City, NV 89005

Commission of the European
Communities
200 Rue de la Loi
B-1049 Brussels
Belgium

Lincoln County Commission
Lincoln County
P.O. Box 90
Pioche, NV 89043

Community Planning & Development
City of North Las Vegas
P.O. Box 4086
North Las Vegas, NV 89030

City Manager
City of Henderson
Henderson, NV 89015

ONWI Library
Battelle Columbus Laboratory
Office of Nuclear Waste Isolation
505 King Avenue
Columbus, OH 43201

Librarian
Los Alamos Technical
Associates, Inc.
P.O. Box 410
Los Alamos, NM 87544

Lawrence Berkeley Laboratory (2)
Earth Sciences Division
University of California
Berkeley, CA 94720
Attn: J. S. Y. Wang
T. N. Narasimhan

6300 R. W. Lynch
6310 T. O. Hunter
6310 NNWSICF
6310 22/12141/64-5958/REP/Q3(XREF)
6310 100/12141/SAND87-7070/Q3
6311 A. L. Stevens
6311 C. Mora
6312 F. W. Bingham
6312 P. C. Kaplan
6313 T. E. Blejwas
6314 J. R. Tillerson
6315 T. O. Hunter, Actg.
6316 R. P. Sandoval
6317 S. Sinnock
6332 WMT Library (20)
6410 N. R. Ortiz
3141 S. A. Landenberger (5)
3151 W. I. Klein (3)
8024 P. W. Dean
3154-3 C. H. Dalin (8)
for DOE/OSTI